



A general, implicit, finite-strain FE² framework for the simulation of dynamic problems on two scales

Erik Tamsen^{1,2} · Daniel Balzani²

Received: 10 January 2020 / Accepted: 14 February 2021 / Published online: 18 March 2021
© The Author(s) 2021

Abstract

In this paper we present a fully-coupled, two-scale homogenization method for dynamic loading in the spirit of FE² methods. The framework considers the balance of linear momentum including inertia at the microscale to capture possible dynamic effects arising from micro heterogeneities. A finite-strain formulation is adapted to account for geometrical nonlinearities enabling the study of e.g. plasticity or fiber pullout, which may be associated with large deformations. A consistent kinematic scale link is established as displacement constraint on the whole representative volume element. The consistent macroscopic material tangent moduli are derived including micro inertia in closed form. These can easily be calculated with a loop over all microscopic finite elements, only applying existing assembly and solving procedures. Thus, making it suitable for standard finite element program architectures. Numerical examples of a layered periodic material are presented and compared to direct numerical simulations to demonstrate the capability of the proposed framework. In addition, a simulation of a split Hopkinson tension test showcases the applicability of the framework to engineering problems.

Keywords Computational homogenization · Multiscale dynamics · Microscopic inertia · RVE · Volume constraint · Consistent tangent modulus

1 Introduction

Under dynamic loading, micro-heterogeneities can give rise to additional wave effects at the microscale leading to complex microscopic stress distributions. This then contributes to the complex macroscopic dynamic material behavior. There are various examples from different fields of application which cover a broad range of length scales. Currently the interest is high in metamaterials in general, but especially in locally resonant metamaterials exhibiting special properties like band gaps and negative bulk moduli. The applications range from cloaking devices [8,24] over tunable sound attenuation [29,34] to earthquake protection [5,43]. More classical materials are being investigated as well. One example is metaconcrete, which replaces aggregates by rubber-coated lead inclusions to weaken impact waves [26,44]. A different

approach for an improved impact resistance are strain-hardening cement-based composites (SHCC), that show a pronounced energy dissipation under dynamic loading, as well as a change in fiber failure and overall crack pattern [10–12]. In addition to that, porous materials have shown an influence of microscopic inertia on voids under high strain rates [45,53]. This list serves only to illustrate the possible influence of the material microstructure on the macroscopic response under high dynamic loading for a wide range of materials and applications. In general, any material under impact loading, which has large variation in stiffness, e.g. rubber-coated particles, or materials with a pronounced variation in density, e.g. if pores or cracks are present at the microscale, can exhibit distinct effective macroscopic properties resulting from the dynamics in the microstructure. In principle, locally large deformations may occur at the microscale in such materials. One example is the fiber-pullout process in SHCC under dynamic loading. Due to the progress of cracks through the cementitious matrix, structural problems arise at the microscale with deformations which are large compared to the structural components such as the fibers or the crack. This requires the consideration of finite

✉ Daniel Balzani
daniel.balzani@rub.de

¹ Institute of Mechanics and Shell Structures, Technische Universität Dresden, 01062 Dresden, Germany

² Chair of Continuum Mechanics, Ruhr University Bochum, 44801 Bochum, Germany

strains in a geometrically nonlinear setting where the description is not limited to linearized strains.

To model the before-mentioned effects, the dynamics at the microscale need to be accounted for. Computational homogenization methods for quasi-static loading have become a common tool in numerical material analysis, see e.g. [15,16,40,46,55,59]. A recent overview of computational homogenization methods in general is given in [18]. In addition a recapitulation of the FE^2 method in particular is presented in [54]. However, with the rise in interest in metamaterials more and more dynamic homogenization frameworks have been published in the last years. Early works date back to elastodynamic problems [62], with more recent work confirming that the effective macroscopic density under the influence of inertia is not the simple average density as for quasi static applications, c.f. [37,41]. Then there are works dealing with microdynamics analytically [64,67], motivating further research. One widely applied homogenization method is asymptotic expansion, see e.g., [7,17,20–22], which is mainly based on the original work of Bensoussan et al. [1]. In addition to that, there is the more general theory of elastodynamic homogenization by Willis [63], which has been applied in e.g. [42,47,49,65] and others. The two approaches are based on related ideas and their similarities are studied in [48]. Both mentioned methods are limited to elastic, periodic media, a considerable limitation when dealing with various composites. A further approach is based on the work of Irving and Kirkwood [23]. It is called the continuum homogenization theory, where the main extensive quantities as mass, momentum and energy are computed as weighted averages of their microscopic counterparts, c.f. [35,38]. A more general approach is the micro-macro simulation based on a representative volume element (RVE). In such homogenization methods, macroscopic quantities such as the deformation gradient and the displacement vector at a macroscopic integration point are projected onto a microscopic boundary value problem whose homogenized response replaces the constitutive material law. In the case where the finite element method (FEM) is used on both scales, this procedure is called the FE^2 method. A good theoretic introduction to this theory including dynamics is given by [14], which has been the foundation on which this paper is built. The framework in [17] calculates a quasi-static microstructure but then applies an inertia-induced eigenstrain based on the microstructure as an extra body force at the macroscale to account for micro-inertia effects. This was extended by [25] to account for matrix cracking at the microscale under impact loading. Other, rather FE^2 -type schemes as [32,33,51,52,56,60,61] calculate the full balance of linear momentum at the microscale. In [32] an explicit, periodic, small-strain framework is presented, which was extended to an implicit time integration method for modeling resonant elastic metamaterials in [33].

[51,52] use the assumption of linear elasticity to improve the computational performance, by splitting the problem into a purely static and a special dynamic boundary value problem (BVP). To better capture a wider range of applied frequencies, [56] use a Floquet–Bloch transformation to build a base of eigenmodes to analyze elastic, periodic metamaterials. The mentioned frameworks all use at least one of the following idealizations: small strains, linear elasticity, periodic or symmetric microstructures. In addition, many require quite elaborate implementations. A recent publication [60] does fulfill the named requirements, however for the derivation of the macroscopic tangent moduli, specific nodes are assumed to experience no microscale fluctuation. This assumption is quite reasonable in the context of metamaterials, whose analysis was primary goal in [60], because there the regions at the unitcell boundaries are particularly stiff. For microscopic problems not specifically addressing classical metamaterial microstructures, however, more flexibility at the boundaries may be more reasonable which is why we propose an alternative approach here.

The aim of this paper is to build a multiscale framework for dynamic loading as general as possible, while still being compatible with standard FE architecture. To enable the analysis of micro-mechanical processes as plasticity or fiber pullout, as well as to incorporate effects resulting from geometric nonlinearities, the proposed framework uses a finite-strain formulation. Its importance is supported by the analytical example in [27] of a nonlinear, elastic metamaterial, where finite strains were shown to be relevant for large wave amplitudes. The conducted numerical studies are so far not specifically chosen to highlight this aspect of the framework. To permit a flexible damage evolution in the RVE, which is not dominated by periodic boundary conditions [6] or aforementioned assumptions regarding fixated fluctuations at specific boundary nodes [60], we propose to apply kinematic scale links as constraints on the whole RVE. This allows us to model any type of RVE morphology.

The paper starts by discussing the general ideas of the framework in Sect. 2. The used notations of the large-strain framework are presented and the averaging relations derived in [13] are briefly recapitulated to include the full balance of momentum at the microscale. Then in Sect. 3 the FE formulations of the microscale are presented and the kinematic constraints are derived. In Sect. 4 the respective macroscale formulations are displayed. There, a focus is laid on the derivation of consistent macroscale tangent moduli in closed form. These enable a quadratically converging macroscopic Newton-iteration, resulting in a robust and efficient algorithm compared to numerical differentiation through perturbation of the macroscopic quantities [39]. Once the whole theoretical background of the framework is explained, Sect. 5 provides numerical examples, demonstrating the convergence behavior and analyzing some properties of RVEs under

dynamic loading. In Sect. 6, the applicability of the framework to construction materials is given. A split Hopkinson tension test is conducted on a sample of strain-hardening cementitious composite (SHCC). The presented example is an extension of the example published in [58], presenting a more complex, 3D microstructure. The publication [58] is focused on the comparison to experimental results and the understanding of the composite behavior, without going into detail on the developed homogenization framework. The paper is completed in Sect. 7 with concluding remarks.

2 Homogenization framework including microscopic inertia

The general idea of the homogenization framework for dynamics is to consider the full balance of linear momentum including the inertia terms at the microscale. This enables not only the analysis of full dynamic fields at the microscale but a direct study of microscopic inertia effects on the macroscale. By using appropriate averaging relations and kinematic links, a consistent scale bridging for dynamic loading is established. In the FE² method, each macroscopic Gauss point is associated with a separate microscopic RVE simulation which uses the macroscopic mechanical quantities to define the microscopic BVP. In order to differentiate the two scales, variables associated with the macroscale are denoted with a bar $\bar{\bullet}$. Here, the finite-strain framework is taken into account in order to enable the analysis of a wide range of material behavior and micro-mechanical effects under dynamic loading. In the following sections the fundamental ingredients of the scale-coupling framework are explained, see also the schematic illustration in Fig. 1.

2.1 Kinematics at different scales

The connection of the (undeformed) reference and the (deformed) current configuration is described by the displacement \mathbf{u} as $\mathbf{u} = \mathbf{x} - \mathbf{X}$, where $\mathbf{X} \in \mathcal{B}$ denotes the coordinates in the reference configuration and $\mathbf{x} \in \mathcal{S}$ the deformation. The link between the two configurations in terms of transformations of vector elements is described by the deformation and displacement gradients, respectively $\mathbf{F} = \partial_{\mathbf{X}}\mathbf{x} = \mathbf{1} + \mathbf{H}$ and $\mathbf{H} = \partial_{\mathbf{X}}\mathbf{u}$, such that $\mathbf{x} = \mathbf{F}\mathbf{X}$. In this work, the origin of the microscopic coordinates is chosen as the geometrical center of the RVE, with

$$\int_{\mathcal{B}} \mathbf{X} \, dV = \mathbf{0}, \tag{1}$$

where $\int_{\mathcal{B}} dV$ is the volume integral over the microscopic reference body \mathcal{B} . Note that this choice of origin has no influence on the results but it simplifies the notation. Now

the microscopic deformation \mathbf{x} can be split into the sum of terms,

$$\mathbf{x} = \bar{\mathbf{u}} + \bar{\mathbf{F}}\mathbf{X} + \tilde{\mathbf{u}}. \tag{2}$$

Herein, two terms result directly from the macroscale: a constant part $\bar{\mathbf{u}}$, which describes the macroscopic rigid body translations, and a homogeneous part $\bar{\mathbf{F}}\mathbf{X}$, defined in terms of the macroscopic deformation gradient.

The difference of these homogeneous deformations $\bar{\mathbf{u}} + \bar{\mathbf{F}}\mathbf{X}$ to the actual deformations \mathbf{x} is the microscopic displacement fluctuation field $\tilde{\mathbf{u}}$. This is the field the microscopic BVP will be solved for. Now the microscopic displacements \mathbf{u} can be written as

$$\mathbf{u} = \bar{\mathbf{u}} + \bar{\mathbf{H}}\mathbf{X} + \tilde{\mathbf{u}}. \tag{3}$$

Analogously, the microscopic deformation gradient can be split as

$$\mathbf{F} = \bar{\mathbf{F}} + \tilde{\mathbf{H}} \quad \text{with} \quad \tilde{\mathbf{H}} = \partial_{\mathbf{X}}\tilde{\mathbf{u}}. \tag{4}$$

At the macroscale the kinematics are standard, see Fig. 2, where the kinematic relations for both the micro- and macroscale are illustrated.

2.2 Averaging relations

To expand quasi-static homogenization frameworks to the case of dynamics, an extended version of the Hill–Mandel condition of macro homogeneity [19,36], which takes into account inertia and body forces at the microscale, is adopted

$$\bar{\mathbf{P}} : \delta\bar{\mathbf{F}} - \bar{\mathbf{f}} \cdot \delta\bar{\mathbf{u}} = \langle \mathbf{P} : \delta\mathbf{F} - \mathbf{f} \cdot \delta\mathbf{u} \rangle, \tag{5}$$

see [3] and [14]. Herein, $\langle \bullet \rangle = \frac{1}{V} \int_{\mathcal{B}} \bullet \, dV$ is an expression used to abbreviate the volume average of a microscopic quantity. \mathbf{P} is the first Piola–Kirchhoff stress tensor, \mathbf{f} is the microscopic body force vector, and $\bar{\mathbf{f}}$ is its macroscopic counterpart. The variational Eq. (5) is also called the Principle of Multiscale Virtual Power. It ensures that the virtual work of the macroscale coincides with its respective microscopic volume average, thus ensuring energetic consistency across the scales. By decomposing $\delta\mathbf{F}$ and $\delta\mathbf{u}$, following (3) and (4), three important equations can be derived. First, one obtains

$$\langle \mathbf{P} : \delta\tilde{\mathbf{F}} - \mathbf{f} \cdot \delta\tilde{\mathbf{u}} \rangle = 0, \tag{6}$$

which is automatically fulfilled for mechanical equilibrium. Then, more importantly, the averaging equation for the effective macroscopic stress $\bar{\mathbf{P}}$ and the effective macroscopic body force vector $\bar{\mathbf{f}}$ are derived as

$$\bar{\mathbf{P}} = \langle \mathbf{P} - \mathbf{f} \otimes \mathbf{X} \rangle \quad \text{and} \tag{7}$$

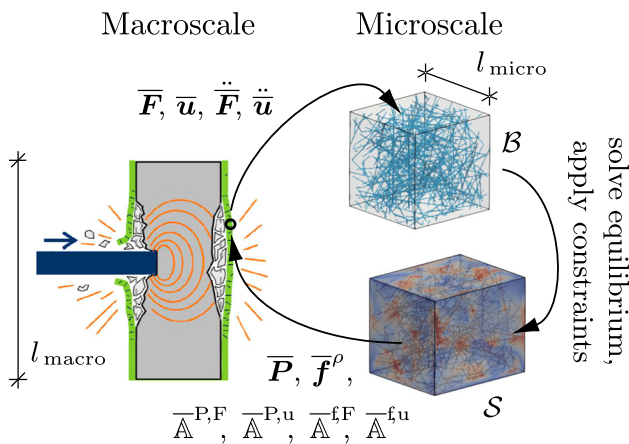


Fig. 1 Overview of the FE² framework including microscale dynamics. Here, an example of macroscopic impact on SHCC is illustrated

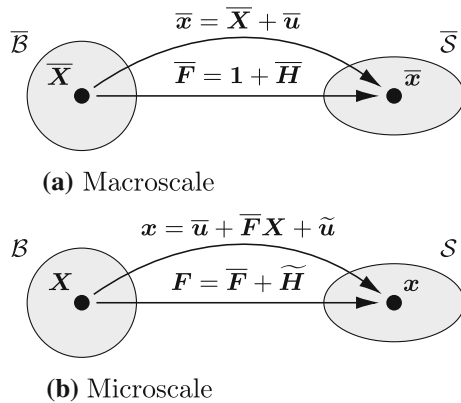


Fig. 2 Large-strain continuum mechanics on both scales

$$\bar{f} = \langle f \rangle. \tag{8}$$

These averaging relations can be found in multiple frameworks dealing with homogenization of dynamics, see e.g., [14,31,32,45,51,52,60]. It was shown in [30] that the extended Hill–Mandel averaging relation can be applied in a discretized setting without introducing additional error by scale transition.

2.3 Scale separation

A principal ingredient of the Hill–Mandel condition, as well as the presented extension (5), is the assumption of scale separation. This means that the equation only holds if the length scale of the microscopic mechanical fields is significantly smaller than the one of the macroscopic mechanical fields. For dynamic homogenization this means in practice, that the macroscopic wavelength is sufficiently larger than the size of the RVE.

2.4 Time integration

In this paper, an implicit numerical time integration method of first order is applied. Considering

$$\ddot{\bullet} = \frac{(\alpha_1 \bullet - \alpha_2 \hat{\bullet})}{\Delta t^2}, \tag{9}$$

we can express the second time derivative of any quantity \bullet as the difference of the current time step and the last $\hat{\bullet}$, divided by the square of the time step Δt , bearing in mind that $\hat{\bullet}$ includes the first and second time derivatives of the last time step. The parameters α_1 and α_2 define the specific time integration scheme. For an explicit time integration, α_1 can be set to zero. Applying this to derivatives of acceleration terms with respect to a quantity \square in the current configuration leads to

$$\frac{\partial \ddot{\bullet}}{\partial \square} = \frac{1}{\Delta t^2} \frac{\partial (\alpha_1 \bullet - \alpha_2 \hat{\bullet})}{\partial \square} = \frac{\alpha_1}{\Delta t^2} \frac{\partial \bullet}{\partial \square}. \tag{10}$$

Analogously, the derivative of a value \bullet with respect to the second time derivative $\ddot{\square}$ reads

$$\frac{\partial \bullet}{\partial \ddot{\square}} = \left(\frac{\partial \ddot{\square}}{\partial \bullet} \right)^{-1} = \left(\frac{1}{\Delta t^2} \frac{\alpha_1 \partial (\square - \alpha_1 \hat{\square})}{\partial \bullet} \right)^{-1} = \frac{\Delta t^2}{\alpha_1} \frac{\partial \bullet}{\partial \square}. \tag{11}$$

For the numerical simulations in the numerical analysis section the widely used Newmark method [50] is applied, with $\alpha_1 = \frac{1}{\beta}$. Herein, β is one of the two parameters of the Newmark method influencing the type and stability of the time integration.

3 The microscopic problem

We start with the formulation of the microscopic problem, which includes the necessary kinematic links to the macroscale. Furthermore, an algorithmic treatment for the associated constraint conditions is given.

3.1 Microscopic balance of linear momentum

For a dynamic analysis, the microscopic balance of linear momentum is given by

$$\text{Div } P + f = 0. \tag{12}$$

The body force vector f can be decomposed into an inertia part f^ρ and a body force vector representing e.g. the gravitational pull f^b . As this framework is intended to model impact loading, gravitational forces are assumed to be negligible compared to the inertia forces. Thus, the relevant body

force vector is defined as $\mathbf{f} := \mathbf{f}^p = -\rho_0 \ddot{\mathbf{u}}$ with ρ_0 referring to the density of the microscale constituents in the reference configuration. If gravitational forces have to be considered, they can be included in the standard way by the additional force vector $\mathbf{f}^b = \rho_0 \mathbf{g}$, where \mathbf{g} is the gravitation field. Since this force however, does not depend on the displacements, it does not represent any specialty with view to the proposed homogenization framework and is thus omitted from the presentation to avoid unnecessary complications.

Using standard FE procedures for the discretization and linearization of the weak form of the balance of linear momentum, the well-known equation

$$\delta \tilde{\mathbf{D}}^T \hat{\mathbf{K}} \Delta \tilde{\mathbf{D}} = \delta \tilde{\mathbf{D}}^T \hat{\mathbf{R}} \tag{13}$$

is obtained, where $\hat{\mathbf{K}}$ and $\hat{\mathbf{R}}$ are the global tangent stiffness matrix and the residuum matrix, respectively. In the following, the hat $\hat{\bullet}$ is used to highlight quantities that include dynamic terms. After incorporating the Dirichlet boundary conditions, the global matrix of incremental nodal displacements $\Delta \tilde{\mathbf{D}}$ are computed from $\hat{\mathbf{K}} \Delta \tilde{\mathbf{D}} = \hat{\mathbf{R}}$ in each Newton iteration step in order to obtain the updated displacements until convergence of the Newton scheme is achieved, i.e. until $|\Delta \tilde{\mathbf{D}}| < tol$. For the classical scheme, the global tangent stiffness matrix $\hat{\mathbf{K}}$ is assembled from the element matrix defined as

$$\hat{\mathbf{k}}^e = \mathbf{k}^e + \frac{\alpha_1}{\Delta t^2} \mathbf{m}^e, \text{ with} \tag{14}$$

$$\mathbf{k}^e = \int_{\mathcal{B}^e} \mathbf{B}^{eT} \mathbb{A} \mathbf{B}^e dV \text{ and } \mathbf{m}^e = \int_{\mathcal{B}^e} \mathbf{N}^e \rho_0 \mathbf{N}^{eT} dV. \tag{15}$$

Herein, \mathbf{N}^e is the classical element matrix of shape functions, \mathbf{B}^e denotes the classical B-matrix containing the derivatives of the shape functions, and \mathbb{A} is the matrix representation of the material tangent modulus, defined as the sensitivity of the microscopic stress with respect to the microscopic deformation gradient as $\mathbb{A} = \partial_{\mathbf{F}} \mathbf{P}$. Analogously, the global residuum matrix $\hat{\mathbf{R}}$ is obtained by the assembly of the element-wise counterparts, given as

$$\hat{\mathbf{r}}^e = \int_{\mathcal{B}^e} (\mathbf{B}^{eT} \mathbf{P} + \mathbf{N}^e \rho_0 \ddot{\mathbf{u}}) dV. \tag{16}$$

Herein, \mathbf{P} denotes the matrix representation of the first Piola–Kirchhoff stresses. It can be noted that both, $\hat{\mathbf{k}}^e$ and $\hat{\mathbf{r}}^e$ have dynamic terms related to the density ρ_0 , which directly enables the evaluation of inertia at the microscale.

3.2 Kinematic links to the macroscale

As depicted in Fig. 1, the macroscopic displacements and deformation gradient and their time derivatives are used to define boundary conditions on the RVE. Inserting them

into (2) is only the first step. If no additional constraint is considered, the BVP will find an equilibrium where the fluctuations $\tilde{\mathbf{u}}$ oppose the applied displacements which results in zero effective displacement of the microstructure. This might not seem obvious at first, however without any imposed constraint, the energetically most favorable position of each node will be its initial configuration, as any deviation from it requires energy. Thus, resulting in a microscopic displacement fluctuation field of $\tilde{\mathbf{u}} = \bar{\mathbf{u}} + \overline{\mathbf{H}}\mathbf{X}$, c.f. (3). Based on the principal of kinematic admissibility, described in detail in [3] and applied in dynamic settings e.g. in [14,52], two kinematic links are chosen here, i.e.

$$\overline{\mathbf{F}} = \langle \mathbf{F} \rangle \text{ and } \bar{\mathbf{u}} = \langle \mathbf{u} \rangle. \tag{17}$$

The first constraint (17)₁ is well-known from quasi-static RVE homogenization frameworks. It postulates, that the volume average of the microscopic deformation gradients must equal the macroscopic deformation gradient. This is usually enforced by choosing appropriate boundary conditions, e.g., linear displacement or periodic boundary conditions. The second constraint (17)₂ is a necessary expansion for the dynamic microscopic problem. This link to the macroscopic displacements is essential in order to prevent the RVE from moving arbitrarily in space. In quasi-static calculations, fluctuations e.g. of a corner node in the RVE are restricted, which does not influence the results. This is, however, not directly possible for the dynamic case without artificially restricting the fluctuations. This is due to the fact that the microscopic deformations are already influenced by just moving the RVE. Thus, restricting the movement at selected locations will yield different deformation fields. Some dynamic homogenization frameworks, e.g. the one in [51], apply a displacement constraint only on the boundary, which can be a reasonable assumption for dynamic metamaterials. There, the boundary lies in the matrix phase, which behaves quasi statically compared to the dynamically active inclusions. The framework proposed here does not make any a priori assumptions on which part of the microstructure will be dynamically significant, as this cannot always be determined in advance for arbitrary problems. Using the displacement split (3) and the definition of the origin of the local coordinate system as the center of the volume (1), the displacement constraint (17)₂ can be reduced to

$$\langle \tilde{\mathbf{u}} \rangle = \mathbf{0}, \tag{18}$$

which states that the constraint is fulfilled, once the volume average of the fluctuations equals zero.

3.3 Algorithmic treatment of kinematic constraints

To enforce the displacement constraint in (18) on the whole RVE domain, we propose to use the method of Lagrange multipliers [2]. Similar applications can be found in [4,52]. For this purpose, the mechanical boundary value problem is recast in terms of the principle of minimum potential energy. By adding the potential Π^λ associated with the Lagrange multipliers λ and the constraint (18) to the function of potential energy Π , one obtains

$$\Pi = \Pi^{\text{int}} + \Pi^{\text{ext}} + \Pi^\lambda, \quad \text{with} \quad \Pi^\lambda = \lambda \cdot \int_{\mathcal{B}} \tilde{\mathbf{u}} \, dV. \quad (19)$$

In the following, only the terms concerning the Lagrange multiplier will be regarded, as the other terms capturing the internal potential energy Π^{int} and the external potential energy Π^{ext} will result in the standard FE formulation (13) described above. However, note that due to the Lagrange term, the additional degrees of freedom λ appear.

3.3.1 Variation

The potential energy is varied once with respect to the displacement fluctuations $\tilde{\mathbf{u}}$ and once with respect to the Lagrange multipliers λ , i.e.

$$\delta_{\tilde{\mathbf{u}}} \Pi^\lambda = \lambda \cdot \int_{\mathcal{B}} \delta \tilde{\mathbf{u}} \, dV \quad \text{and} \quad (20)$$

$$\delta_\lambda \Pi^\lambda = \delta \lambda \cdot \int_{\mathcal{B}} \tilde{\mathbf{u}} \, dV. \quad (21)$$

3.3.2 Discretization

Using $\tilde{\mathbf{u}} \approx N^e \tilde{\mathbf{d}}^e$ and $\delta \tilde{\mathbf{u}} \approx N^e \delta \tilde{\mathbf{d}}^e$ as FE approximations, the discretized expressions can be written as

$$\delta_{\tilde{\mathbf{u}}} \Pi^\lambda = \lambda^T \mathbf{A}_e \left[\int_{\mathcal{B}^e} N^e \, dV \delta \tilde{\mathbf{d}}^e \right] \quad \text{and} \quad (22)$$

$$\delta_\lambda \Pi^\lambda = \delta \lambda^T \mathbf{A}_e \left[\int_{\mathcal{B}^e} N^e \, dV \tilde{\mathbf{d}}^e \right]. \quad (23)$$

To obtain the equivalent of the global volume integral in terms of the elements, the assembly operator \mathbf{A} is applied for the respective matrices. For better readability, a new element matrix is defined as

$$\mathbf{g}^{eT} = \int_{\mathcal{B}^e} N^e \, dV. \quad (24)$$

This simplifies the formulations to

$$\delta_{\tilde{\mathbf{u}}} \Pi^\lambda = \lambda^T \mathbf{A}_e \left[\mathbf{g}^{eT} \delta \tilde{\mathbf{d}}^e \right] \quad \text{and} \quad (25)$$

$$\delta_\lambda \Pi^\lambda = \delta \lambda^T \mathbf{A}_e \left[\mathbf{g}^{eT} \tilde{\mathbf{d}}^e \right]. \quad (26)$$

3.3.3 Global matrix notation

To write the whole system of equations as a global problem, the global matrices are defined in terms of the element matrices, i.e.

$$\mathbf{G} = \mathbf{A} \mathbf{g}^e, \quad \tilde{\mathbf{D}} = \mathbf{U}_e \tilde{\mathbf{d}}^e \quad \text{and} \quad \delta \tilde{\mathbf{D}} = \mathbf{U}_e \delta \tilde{\mathbf{d}}^e, \quad (27)$$

where \mathbf{A} is the aforementioned assembly operator and \mathbf{U} a unification operator, as the node displacement fluctuations shared by different elements are not added up, but belong to the same degree of freedom. Now the expressions (25) and (26) can be reformulated in global fields as

$$\delta_{\tilde{\mathbf{u}}} \Pi^\lambda = \lambda^T \mathbf{G}^T \delta \tilde{\mathbf{D}} = \delta \tilde{\mathbf{D}}^T \mathbf{G} \lambda \quad \text{and} \quad (28)$$

$$\delta_\lambda \Pi^\lambda = \delta \lambda^T \mathbf{G}^T \tilde{\mathbf{D}} = \mathbf{0}. \quad (29)$$

Since the Lagrange multiplier only appears in Π^λ , no terms result from the variation of Π^{int} and Π^{ext} with respect to λ . It follows, that the second expression has to vanish, see (29).

3.3.4 Linearization

In order to solve the nonlinear global system of equations, the Newton–Raphson method is utilized. For that purpose, we not only need the equations in weak form as in (28) and (29) but also their linearizations. They are used to iteratively compute the nodal displacement fluctuations as well as the Lagrange multipliers. Here the definition of the Δ operator is used. When linearizing a function $f(x) = 0$ at \hat{x} as $\text{Lin} f = f|_{\hat{x}} + \Delta f|_{\hat{x}}$, then $\Delta f = \left. \frac{\partial f}{\partial x} \right|_{\hat{x}} \Delta x$. Applying this to the weak forms results in

$$\text{Lin} \delta_{\tilde{\mathbf{u}}} \Pi^\lambda = \delta \tilde{\mathbf{D}}^T \mathbf{G} \lambda + \delta \tilde{\mathbf{D}}^T \mathbf{G} \Delta \lambda \quad \text{and} \quad (30)$$

$$\text{Lin} \delta_{\lambda_1} \Pi^\lambda = \delta \lambda^T \mathbf{G}^T \tilde{\mathbf{D}} + \delta \lambda^T \mathbf{G}^T \Delta \tilde{\mathbf{D}} = \mathbf{0}. \quad (31)$$

3.4 Global discretized microscopic problem including constraint

From the linearized variations of Π^λ we define the global residua

$$\mathbf{R}^{\tilde{\mathbf{u}}} = -\mathbf{G} \lambda = \sum_e \mathbf{r}^{\tilde{\mathbf{u}}e} \quad \text{with} \quad \mathbf{r}^{\tilde{\mathbf{u}}e} = -\mathbf{g}^e \lambda \quad \text{and} \quad (32)$$

$$\mathbf{R}^\lambda = -\mathbf{G}^T \tilde{\mathbf{D}} = \sum_e \mathbf{r}^{\lambda e} \quad \text{with} \quad \mathbf{r}^{\lambda e} = -\mathbf{g}^{eT} \tilde{\mathbf{d}}^e. \quad (33)$$

Including all linearized variations of $\Pi^{\text{int}} + \Pi^{\text{ext}} + \Pi^\lambda$ yields the discrete equation

$$\begin{bmatrix} \delta \tilde{\mathbf{D}}^T | \delta \lambda^T \end{bmatrix} \begin{bmatrix} \hat{\mathbf{K}} | \mathbf{G} \\ \mathbf{G}^T | \mathbf{0} \end{bmatrix} \begin{bmatrix} \Delta \tilde{\mathbf{D}} \\ \Delta \lambda \end{bmatrix} = \begin{bmatrix} \delta \tilde{\mathbf{D}}^T | \delta \lambda^T \end{bmatrix} \begin{bmatrix} \hat{\mathbf{R}} + \mathbf{R}^{\tilde{u}} \\ \mathbf{R}^\lambda \end{bmatrix} \tag{34}$$

as expansion of (13). After including Dirichlet boundary conditions and applying standard arguments of variational calculus, the resulting discrete system of equations reads

$$\begin{bmatrix} \hat{\mathbf{K}} | \mathbf{G} \\ \mathbf{G}^T | \mathbf{0} \end{bmatrix} \begin{bmatrix} \Delta \tilde{\mathbf{D}} \\ \Delta \lambda \end{bmatrix} = \begin{bmatrix} \hat{\mathbf{R}} + \mathbf{R}^{\tilde{u}} \\ \mathbf{R}^\lambda \end{bmatrix}. \tag{35}$$

Note that in contrast to \mathbf{K} , the new tangent stiffness matrix is not necessarily positive definite, which needs to be taken into account when choosing and setting up a solver. In general, Lagrange multipliers have the disadvantage of adding new degrees of freedom to the system of equations. For the presented displacement constraint, only one extra degree of freedom is added for each spacial direction. This is due to the fact that the constraint is applied on the whole RVE which avoids the approximation of the Lagrange multipliers as field variables. Thus, for three-dimensional problems, λ will only add three additional degrees of freedom. Compared to the displacement fluctuations which are linked to the nodes and which may thus easily reach thousands of degrees of freedom, the number of three additional degrees of freedom over the whole RVE is negligible, making it computationally cheap.

3.5 Coupling of the deformation gradient

The constraint related to the deformation gradient (17)₁, can be derived and applied in the same manner as just presented for (17)₂ in the previous section. The only change in the final formulation is that the related $\mathbf{g}_{(\mathbf{F})}^{eT}$ matrix needs to be computed as the volume average of the element B-Matrix instead of the shape functions,

$$\mathbf{g}_{(\mathbf{F})}^{eT} = \int_{\mathcal{B}^e} \mathbf{B}^e \, dV. \tag{36}$$

Applying the constraint regarding the deformation gradient on the volume instead of enforcing it using periodic boundary conditions will lead to minimally invasive boundary conditions enabling e.g. arbitrary damage propagation without artificial restrictions imposed by periodic boundary conditions. As shown in [13], such minimally invasive boundary conditions result in a softer constraint compared to periodic boundary conditions. To simplify the numerical examples in this paper, only the displacement constraint is applied and the constraint related to the deformation gradient is enforced by using periodic boundary conditions.

4 The macroscopic problem

For the solution of the dynamic macroscopic boundary value problem, the associated linearized, discretized balance equations are derived. Herein, specific macroscopic tangent moduli appear which are consistently derived for the case where the displacement constraint proposed in the previous section is taken into account.

4.1 Macroscopic boundary value problem

4.1.1 Macroscopic equilibrium equation

The complete macroscopic balance of linear momentum including inertia is given by

$$\text{Div } \bar{\mathbf{P}} + \bar{\mathbf{f}} = \mathbf{0}. \tag{37}$$

Applying the Galerkin method with a test function $\delta \bar{\mathbf{u}}$ on the entire domain $\bar{\mathcal{B}}$ leads to the weak form of linear momentum $\int_{\bar{\mathcal{B}}} \delta \bar{\mathbf{u}}^T (\text{Div } \bar{\mathbf{P}} + \bar{\mathbf{f}}) \, dV = 0$. By applying $\text{Div}(\mathbf{P}) \delta \mathbf{u} = \text{Div}(\mathbf{P}^T \delta \mathbf{u}) - \mathbf{P} : \text{Grad } \delta \mathbf{u}$ and the Gauss theorem $\int_{\bar{\mathcal{B}}} \text{Div}(\mathbf{P}^T \delta \mathbf{u}) \, dV = \int_{\partial \bar{\mathcal{B}}} \delta \mathbf{u} \cdot \mathbf{t} \, dA$, the weak form is written as

$$\bar{G} := \int_{\bar{\mathcal{B}}} \delta \bar{\mathbf{F}} : \bar{\mathbf{P}} \, dV + \int_{\bar{\mathcal{B}}} \delta \bar{\mathbf{u}}^T \bar{\mathbf{f}}^\rho \, dV = 0. \tag{38}$$

Herein, zero traction forces are taken into account at the boundary and $\delta \mathbf{F} = \text{Grad } \delta \mathbf{u}$. Analogous to the microscale, only body forces related to inertia, not gravitation, are considered at the macroscale. Thus, the body force vector is set to $\bar{\mathbf{f}} := \bar{\mathbf{f}}^\rho = \langle \mathbf{f}^\rho \rangle$.

4.1.2 Linearization

To solve the weak form of equilibrium by using the standard Newton–Raphson scheme, the linearized balance of linear momentum is obtained as

$$\begin{aligned} \text{Lin } \bar{G} &= \bar{G} + \Delta \bar{G} = 0 \quad \text{with } \Delta \bar{G} \\ &= \int_{\bar{\mathcal{B}}} \delta \bar{\mathbf{F}} : \Delta \bar{\mathbf{P}} \, dV + \int_{\bar{\mathcal{B}}} \delta \bar{\mathbf{u}}^T \Delta \bar{\mathbf{f}}^\rho \, dV. \end{aligned} \tag{39}$$

Now the Δ operator is applied again to $\Delta \bar{\mathbf{P}}$ and $\Delta \bar{\mathbf{f}}^\rho$:

$$\Delta \bar{\mathbf{P}} = \frac{\partial \bar{\mathbf{P}}}{\partial \bar{\mathbf{F}}} : \Delta \bar{\mathbf{F}} + \frac{\partial \bar{\mathbf{P}}}{\partial \bar{\mathbf{u}}} \cdot \Delta \bar{\mathbf{u}} \quad \text{and} \tag{40}$$

$$\Delta \bar{\mathbf{f}}^\rho = \frac{\partial \bar{\mathbf{f}}^\rho}{\partial \bar{\mathbf{F}}} : \Delta \bar{\mathbf{F}} + \frac{\partial \bar{\mathbf{f}}^\rho}{\partial \bar{\mathbf{u}}} \cdot \Delta \bar{\mathbf{u}}. \tag{41}$$

Here an interesting property of the two-scale homogenization framework for dynamics is observed. The macroscopic

stress not only depends on the deformation gradient but on the acceleration as well. In turn, the inertia forces can also depend on the deformation gradient in addition to the acceleration. We define the resulting four sensitivities as

$$\begin{aligned} \overline{\mathbb{A}}^{P,F} &= \partial_{\overline{\mathbf{F}}} \overline{\mathbf{P}}, & \overline{\mathbb{A}}^{P,u} &= \partial_{\ddot{\mathbf{u}}} \overline{\mathbf{P}}, \\ \overline{\mathbb{A}}^{f,F} &= \partial_{\overline{\mathbf{F}}} \overline{\mathbf{f}}^\rho & \text{and} & \quad \overline{\mathbb{A}}^{f,u} = \partial_{\ddot{\mathbf{u}}} \overline{\mathbf{f}}^\rho. \end{aligned} \tag{42}$$

These moduli (42) are inserted into the linearized weak form which results in

$$\begin{aligned} \text{Lin} \overline{G} &= \int_{\overline{\mathcal{B}}} \delta \overline{\mathbf{F}} : \overline{\mathbf{P}} \, dV \\ &+ \int_{\overline{\mathcal{B}}} \delta \overline{\mathbf{u}}^T \overline{\mathbf{f}}^\rho \, dV + \int_{\overline{\mathcal{B}}} \delta \overline{\mathbf{F}} : \overline{\mathbb{A}}^{P,F} : \Delta \overline{\mathbf{F}} \, dV \\ &+ \int_{\overline{\mathcal{B}}} \delta \overline{\mathbf{F}} : \overline{\mathbb{A}}^{P,u} \cdot \Delta \ddot{\mathbf{u}} \, dV + \int_{\overline{\mathcal{B}}} \delta \overline{\mathbf{u}}^T \overline{\mathbb{A}}^{f,F} : \Delta \overline{\mathbf{F}} \, dV \\ &+ \int_{\overline{\mathcal{B}}} \delta \overline{\mathbf{u}}^T \overline{\mathbb{A}}^{f,u} \cdot \Delta \ddot{\mathbf{u}} \, dV. \end{aligned} \tag{43}$$

4.1.3 FE discretization

The linearization is of the weak form of the balance of linear momentum is now discretized in terms of finite elements. First, the linear increment

$$\begin{aligned} \Delta \overline{G} &= \int_{\mathcal{B}} \delta \overline{\mathbf{F}} : \overline{\mathbb{A}}^{P,F} : \Delta \overline{\mathbf{F}} \, dV + \int_{\mathcal{B}} \delta \overline{\mathbf{F}} : \overline{\mathbb{A}}^{P,u} \cdot \Delta \ddot{\mathbf{u}} \, dV \\ &+ \int_{\mathcal{B}} \delta \overline{\mathbf{u}}^T \overline{\mathbb{A}}^{f,F} : \Delta \overline{\mathbf{F}} \, dV + \int_{\mathcal{B}} \delta \overline{\mathbf{u}}^T \overline{\mathbb{A}}^{f,u} \cdot \Delta \ddot{\mathbf{u}} \, dV, \end{aligned} \tag{44}$$

is discretized using standard FE formulations. Then, to get rid of the dependence on the time derivatives, the numerical time integration in terms of (10) is used, which results in

$$\begin{aligned} \Delta \overline{G} &= \sum_{e=1}^{n_{\text{ele}}} \delta \overline{d}_P^e \left(\int_{\mathcal{B}^e} \overline{B}_{ijP}^e \overline{\mathbb{A}}_{ijmn}^{P,F} \overline{B}_{mnQ}^e + \frac{\overline{\alpha}_1}{\Delta t^2} \overline{B}_{ijP}^e \overline{\mathbb{A}}_{ijk}^{P,u} \overline{N}_{Qk}^e \right. \\ &\left. + \overline{N}_{Pi}^e \overline{\mathbb{A}}_{imn}^{f,F} \overline{B}_{mnQ}^e + \frac{\overline{\alpha}_1}{\Delta t^2} \overline{N}_{Pi}^e \overline{\mathbb{A}}_{ik}^{f,u} \overline{N}_{Qk}^e \, dV \right) \Delta \overline{d}_Q^e. \end{aligned} \tag{45}$$

Herein, the matrix representation of the moduli in index notation has been used. Lowercase indices refer the spatial dimension n_{dm} , whereas uppercase indices to the total degrees of freedom of a element n_{edf} . Again, standard element B-matrix \overline{B}^e and shape function matrix \overline{N}^e are considered. By extracting the nodal virtual and incremental displacements, this yields the definition of the full macroscopic element tangent stiffness matrix

$$\widehat{k}_{PQ}^e = \int_{\mathcal{B}^e} \left(\overline{B}_{ijP}^e \overline{\mathbb{A}}_{ijmn}^{P,F} \overline{B}_{mnQ}^e + \frac{\overline{\alpha}_1}{\Delta t^2} \overline{B}_{ijP}^e \overline{\mathbb{A}}_{ijk}^{P,u} \overline{N}_{Qk}^e \right.$$

$$\left. + \overline{N}_{Pi}^e \overline{\mathbb{A}}_{imn}^{f,F} \overline{B}_{mnQ}^e + \frac{\overline{\alpha}_1}{\Delta t^2} \overline{N}_{Pi}^e \overline{\mathbb{A}}_{ik}^{f,u} \overline{N}_{Qk}^e \right) \, dV. \tag{46}$$

Now the remaining part of the linearization (43), the residuum \overline{R} , is discretized as

$$\widehat{R} = \sum_{e=1}^{n_{\text{ele}}} \left(\delta \overline{d}_P \int_{\mathcal{B}^e} \overline{B}_{ijP}^e \overline{P}_{ij} \, dV + \delta \overline{d}_P \int_{\mathcal{B}^e} \overline{N}_{iP}^e \overline{f}_i^\rho \, dV \right). \tag{47}$$

By extracting the nodal virtual displacements, the element residuum is identified as

$$\widehat{r}_P^e = \int_{\mathcal{B}^e} \left(\overline{B}_{ijP}^e \overline{P}_{ij} + \overline{N}_{Pi}^e \overline{f}_i^\rho \right) \, dV, \tag{48}$$

where again matrix representation and index notation is used.

4.2 Consistent macroscopic tangent moduli

For the dynamic homogenization framework, four macroscopic tangent moduli (42) need to be determined. To obtain the sought-after moduli in closed form, we start with taking the derivative of the incremental linearized weak form of linear momentum at the microscale with respect to the two relevant macroscopic quantities, the deformation gradient $\overline{\mathbf{F}}$ and the acceleration $\ddot{\mathbf{u}}$. Then we derive the moduli by considering the microscopic problem in its equilibrium state.

4.2.1 Incremental weak forms including displacement constraint

As it will be shown later, the derivatives of the microscopic fluctuations with respect to the macroscopic deformation gradient and the acceleration will be required. For their calculation, the incremental linearized weak forms have to be derived with respect to these two quantities. In order to account for the proposed displacement constraint, the associated increments of the weak form of linear momentum and of the Lagrange multiplier potential with respect to the microscopic displacement fluctuations as well as the Lagrange multipliers, i.e. (20) and (21), are identified as

$$\begin{aligned} \Delta G^{\tilde{u}} &= \int_{\mathcal{B}} \delta F_{ij} \mathbb{A}_{ijmn} \Delta F_{mn} \, dV + \int_{\mathcal{B}} \delta \tilde{u}_i \rho_0 \Delta \tilde{u}_i \, dV \\ &+ \Delta \lambda_i \int_{\mathcal{B}} \delta \tilde{u}_i \, dV \quad \text{and} \end{aligned} \tag{49}$$

$$\Delta G^\lambda = \delta \lambda_i \int_{\mathcal{B}} \Delta \tilde{u}_i \, dV. \tag{50}$$

Using the decompositions (3) and (4), equation (49) can be reformulated as

$$\begin{aligned} \Delta G^{\tilde{u}} &= \int_{\mathcal{B}} \delta F_{ij} \mathbb{A}_{ijmn} \Delta \bar{F}_{mn} \, dV \\ &+ \int_{\mathcal{B}} \delta F_{ij} \mathbb{A}_{ijmn} \Delta \tilde{H}_{mn} \, dV + \int_{\mathcal{B}} \delta u_i \rho_0 \Delta \ddot{u}_i \, dV \\ &+ \int_{\mathcal{B}} \delta u_i \rho_0 \Delta \ddot{\bar{F}}_{ij} X_j \, dV + \int_{\mathcal{B}} \delta u_i \rho_0 \Delta \ddot{u}_i \, dV \\ &+ \Delta \lambda_i \int_{\mathcal{B}} \delta \tilde{u}_i \, dV. \end{aligned} \tag{51}$$

4.2.2 Derivatives of incremental weak forms

By taking the derivatives of the increments (50) and (51) in the equilibrium state $\Delta G = 0$, a closed form formulation of the tangent moduli will be obtained later. Thus, the associated derivatives are computed in the following.

Derivative with respect to \bar{F} : Taking the derivatives of (50) and (51) with respect to the macroscopic deformation gradient, while considering (10) results in

$$\begin{aligned} 0_{kl} &= \int_{\mathcal{B}} \delta F_{ij} \mathbb{A}_{ijkl} \, dV + \int_{\mathcal{B}} \delta F_{ij} \mathbb{A}_{ijmn} \frac{\partial \tilde{H}_{mn}}{\partial \bar{F}_{kl}} \, dV \\ &+ \frac{\bar{\alpha}_1}{\Delta t^2} \int_{\mathcal{B}} \delta u_k \rho_0 X_l \, dV \\ &+ \frac{\alpha_1}{\Delta t^2} \int_{\mathcal{B}} \delta u_i \rho_0 \frac{\partial \tilde{u}_i}{\partial \bar{F}_{kl}} \, dV + \frac{\partial \lambda_i}{\partial \bar{F}_{kl}} \int_{\mathcal{B}} \delta \tilde{u}_i \, dV \quad \text{and} \end{aligned} \tag{52}$$

$$0_{kl} = \delta \lambda_i \int_{\mathcal{B}} \frac{\partial \tilde{u}_i}{\partial \bar{F}_{kl}} \, dV. \tag{53}$$

Using standard FE discretization yields

$$\begin{aligned} 0_{kl} &= \sum_{e=1}^{n_{ele}} \delta \tilde{d}_P^e \left(\int_{\mathcal{B}^e} B_{ijP}^e \mathbb{A}_{ijkl} \, dV \right. \\ &+ \int_{\mathcal{B}^e} B_{ijP}^e \mathbb{A}_{ijmn} B_{mnQ}^e \, dV \frac{\partial \tilde{d}_Q^e}{\partial \bar{F}_{kl}} \\ &+ \frac{\bar{\alpha}_1}{\Delta t^2} \int_{\mathcal{B}^e} N_{Pk}^e \rho_0 X_l \, dV \\ &+ \left. \frac{\alpha_1}{\Delta t^2} \int_{\mathcal{B}^e} N_{Pi}^e \rho_0 N_{Qi}^e \, dV \frac{\partial \tilde{d}_Q^e}{\partial \bar{F}_{kl}} + \int_{\mathcal{B}^e} N_{Pi}^e \, dV \frac{\partial \lambda_i}{\partial \bar{F}_{kl}} \right) \quad \text{and} \end{aligned} \tag{54}$$

$$0_{kl} = \sum_{e=1}^{n_{ele}} \delta \lambda_i \left(\int_{\mathcal{B}^e} N_{Pi}^e \, dV \frac{\partial \tilde{d}_P^e}{\partial \bar{F}_{kl}} \right). \tag{55}$$

Rewriting this in global notation using the abbreviations defined in Appendix 1 Table 2 leads to the expressions

$$\mathbf{0} = \mathbf{L} + \frac{\bar{\alpha}_1}{\Delta t^2} \mathbf{Z} + \left(\mathbf{K} + \frac{\alpha_1}{\Delta t^2} \mathbf{M} \right) \frac{\partial \tilde{\mathbf{D}}}{\partial \bar{\mathbf{F}}} + \mathbf{G} \frac{\partial \boldsymbol{\lambda}}{\partial \bar{\mathbf{F}}} \quad \text{and} \tag{56}$$

$$\mathbf{0} = \mathbf{G}^T \frac{\partial \tilde{\mathbf{D}}}{\partial \bar{\mathbf{F}}}. \tag{57}$$

By combining the nodal fluctuations and the Lagrange multipliers into one column matrix \mathbf{D}^* , the two equations can be written as one system of equations $\mathbf{K}^* \partial_{\bar{\mathbf{F}}} \mathbf{D}^* = -\mathbf{L}^*$ with the matrices

$$\mathbf{D}^{*T} = \left[\tilde{\mathbf{D}}^T \mid \boldsymbol{\lambda}^T \right], \tag{58}$$

$$\mathbf{L}^{*T} = \left[\mathbf{L}^T + \frac{\bar{\alpha}_1}{\Delta t^2} \mathbf{Z}^T \mid \mathbf{0} \right] \quad \text{and} \tag{59}$$

$$\mathbf{K}^* = \left[\begin{array}{c|c} \mathbf{K} + \frac{\alpha_1}{\Delta t^2} \mathbf{M} & \mathbf{G} \\ \hline \mathbf{G}^T & \mathbf{0} \end{array} \right]. \tag{60}$$

Then, the required derivative can be computed from

$$\frac{\partial \mathbf{D}^*}{\partial \bar{\mathbf{F}}} = -\mathbf{K}^{*-1} \mathbf{L}^*. \tag{61}$$

Note that \mathbf{K}^* is the microscopic tangent stiffness matrix in (35), which is already available from solving the microscopic boundary value problem.

Derivative with respect to \ddot{u} : Analogously, the derivative of (51) with respect to \ddot{u} can be obtained by applying (11), i.e. one obtains

$$\begin{aligned} 0_k &= \frac{\Delta t^2}{\alpha_1} \int_{\mathcal{B}} \delta F_{ij} \mathbb{A}_{ijmn} \frac{\partial \tilde{H}_{mn}}{\partial \ddot{u}_k} \, dV + \int_{\mathcal{B}} \delta u_k \rho_0 \, dV \\ &+ \int_{\mathcal{B}} \delta u_i \rho_0 \frac{\partial \tilde{u}_i}{\partial \ddot{u}_k} \, dV + \frac{\partial \lambda_i}{\partial \ddot{u}_k} \int_{\mathcal{B}} \delta \tilde{u}_i \, dV \end{aligned} \tag{62}$$

$$0_k = \delta \lambda_i \int_{\mathcal{B}} \frac{\partial \tilde{u}_i}{\partial \ddot{u}_k} \, dV. \tag{63}$$

Standard FE discretization using matrix representation and index notation yields

$$\begin{aligned} 0_k &= \sum_{e=1}^{n_{ele}} \delta \tilde{d}_P^e \left(\int_{\mathcal{B}^e} B_{ijP}^e \mathbb{A}_{ijmn} B_{mnQ}^e \, dV \frac{\partial \tilde{d}_Q^e}{\partial \ddot{u}_k} + \int_{\mathcal{B}^e} N_{Pk} \rho_0 \, dV \right. \\ &+ \left. \frac{\alpha_1}{\Delta t^2} \int_{\mathcal{B}^e} N_{Pi}^e \rho_0 N_{Qi}^e \, dV \frac{\partial \tilde{d}_Q^e}{\partial \ddot{u}_k} + \int_{\mathcal{B}^e} N_{Pi}^e \, dV \frac{\partial \lambda_i}{\partial \ddot{u}_k} \right) \quad \text{and} \end{aligned} \tag{64}$$

$$0_k = \sum_{e=1}^{n_{ele}} \delta \lambda_i \left(\int_{\mathcal{B}^e} N_{Pi}^e \, dV \frac{\partial \tilde{d}_P^e}{\partial \ddot{u}_k} \right). \tag{65}$$

Again, the two equations are combined by joining the displacements and the Lagrange multipliers into a single matrix, c.f. (58). By solving the resulting system of equations with respect to the required derivatives $\partial_{\ddot{u}} \mathbf{D}^*$, we obtain

$$\frac{\partial \mathbf{D}^*}{\partial \ddot{u}} = -\mathbf{K}^{*-1} \mathbf{W}^*. \tag{66}$$

Herein, the definitions (58)–(59), the abbreviations defined in Appendix 1 Table 2, as well as $\mathbf{W}^{*T} = [\mathbf{W}^T \mathbf{0}]$ are used.

4.2.3 Derivation of tangent moduli

In this subsection the four moduli will be derived by inserting the derivatives computed in the last subsection. Note that all moduli are only consistent for a microscopic equilibrium state. Thus, quadratic convergence of the macroscopic Newton–Raphson iteration is only ensured if the microscopic boundary value problem is solved for each macroscopic iteration step. After the last microscopic iteration, the consistent tangent moduli can be computed.

Derivation of $\bar{\mathbb{A}}^{P,F}$: To derive the sensitivity of the macroscopic stresses with respect to the macroscopic deformation gradient, the derivative is rewritten using the definition of the macroscopic stresses in terms of the microscopic fields, i.e.

$$\bar{\mathbb{A}}_{ijmn}^{P,F} = \frac{\partial \bar{P}_{ij}}{\partial \bar{F}_{mn}} = \frac{\partial \langle P_{ij} + \rho_0 \ddot{u}_i X_j \rangle}{\partial \bar{F}_{mn}}. \quad (67)$$

Using the chain rule $\frac{\partial \mathbf{P}(\mathbf{F})}{\partial \mathbf{F}} = \frac{\partial \mathbf{P}}{\partial \mathbf{F}} : \frac{\partial \mathbf{F}}{\partial \mathbf{F}}$, applying (3), (4), (10) and inserting FE discretization, the equation can be written as

$$\begin{aligned} \bar{\mathbb{A}}_{ijmn}^{P,F} = & \sum_{e=1}^{n_{\text{ele}}} \left(\frac{1}{V} \int_{\mathcal{B}^e} \mathbb{A}_{ijmn} \, dV \right. \\ & + \frac{\bar{\alpha}_1}{\Delta t^2} \frac{1}{V} \int_{\mathcal{B}^e} \rho_0 \delta_{im} X_j X_n \, dV \\ & + \frac{1}{V} \int_{\mathcal{B}^e} \mathbb{A}_{ijkl} B_{klP}^e \, dV \frac{\partial \tilde{d}_P^e}{\partial \bar{F}_{mn}} \\ & \left. + \frac{\alpha_1}{\Delta t^2} \frac{1}{V} \int_{\mathcal{B}^e} \rho_0 N_{Pi}^e X_j \, dV \frac{\partial \tilde{d}_P^e}{\partial \bar{F}_{mn}} \right). \quad (68) \end{aligned}$$

By using the global abbreviations defined in Appendix 1 Tables 2, 3 and inserting (61), the closed form result is obtained as

$$\bar{\mathbb{A}}^{P,F} = \left\langle \mathbb{A} + \frac{1}{\beta \Delta t^2} \mathbb{Y} \right\rangle - \frac{1}{V} \mathbf{L}^{*T} \mathbf{K}^{*-1} \mathbf{L}^*. \quad (69)$$

Note that this result has already been presented in [57] for a special scenario of dynamic homogenization, which did not include macroscopic acceleration and the displacement constraint.

Derivation of $\bar{\mathbb{A}}^{P,u}$: The derivation of the sensitivity of the macroscopic stresses with respect to the macroscopic accelerations is analogous to that of $\bar{\mathbb{A}}^{P,F}$. First the derivative is

rewritten using the definition of the macroscopic stresses in terms of the microscopic fields as

$$\bar{\mathbb{A}}_{ijk}^{P,u} = \frac{\partial \bar{P}_{ij}}{\partial \ddot{u}_k} = \frac{\partial \langle P_{ij} + \rho_0 \ddot{u}_i X_j \rangle}{\partial \ddot{u}_k}. \quad (70)$$

Then using the chain rule, (3), (4), (10) and FE discretization, the equation reads

$$\begin{aligned} \bar{\mathbb{A}}_{ijk}^{P,u} = & \sum_{e=1}^{n_{\text{ele}}} \left(\frac{1}{V} \int_{\mathcal{B}^e} \rho_0 \delta_{ik} X_j \, dV + \frac{1}{V} \int_{\mathcal{B}^e} \mathbb{A}_{ijmn} B_{mnP}^e \, dV \frac{\partial \tilde{d}_P^e}{\partial \ddot{u}_k} \right. \\ & \left. + \frac{\alpha_1}{\Delta t^2} \frac{1}{V} \int_{\mathcal{B}^e} \rho_0 X_j N_{Pi}^e \, dV \frac{\partial \tilde{d}_P^e}{\partial \ddot{u}_k} \right). \quad (71) \end{aligned}$$

Finally, using the global abbreviations in Appendix 1 Tables 2, 3 and inserting (66), the modulus is obtained as

$$\bar{\mathbb{A}}^{P,u} = \langle \mathbf{V} \rangle - \frac{1}{V} \mathbf{L}^{*T} \mathbf{K}^{*-1} \mathbf{W}^*. \quad (72)$$

Derivation of $\bar{\mathbb{A}}^{f,F}$: The derivation of the sensitivity of the macroscopic inertia with respect to the macroscopic deformation gradient is again similar to that of $\bar{\mathbb{A}}^{P,F}$. First, the derivative is rewritten as

$$\bar{\mathbb{A}}_{imn}^{f,F} = \frac{\partial \bar{f}_i^{\rho}}{\partial \bar{F}_{mn}} = \frac{\partial \langle \rho_0 \ddot{u}_i \rangle}{\partial \bar{F}_{mn}} \quad (73)$$

and by using (3), (4), (10) and FE discretization, the equation reads

$$\begin{aligned} \bar{\mathbb{A}}_{imn}^{f,F} = & \sum_{e=1}^{n_{\text{ele}}} \left(\frac{\bar{\alpha}_1}{\Delta t^2} \frac{1}{V} \int_{\mathcal{B}^e} \rho_0 \delta_{im} X_n \, dV \right. \\ & \left. + \frac{\alpha_1}{\Delta t^2} \frac{1}{V} \int_{\mathcal{B}^e} \rho_0 N_{Pi}^e \, dV \frac{\partial \tilde{d}_P^e}{\partial \bar{F}_{mn}} \right). \quad (74) \end{aligned}$$

Using the global abbreviations in Appendix 1 Tables 2, 3 and plugging in (61), the modulus is identified as

$$\bar{\mathbb{A}}^{f,F} = \frac{\bar{\alpha}_1}{\Delta t^2} \langle \mathbf{V}^T \rangle - \frac{1}{V} \frac{\alpha_1}{\Delta t^2} \mathbf{W}^{*T} \mathbf{K}^{*-1} \mathbf{L}^*. \quad (75)$$

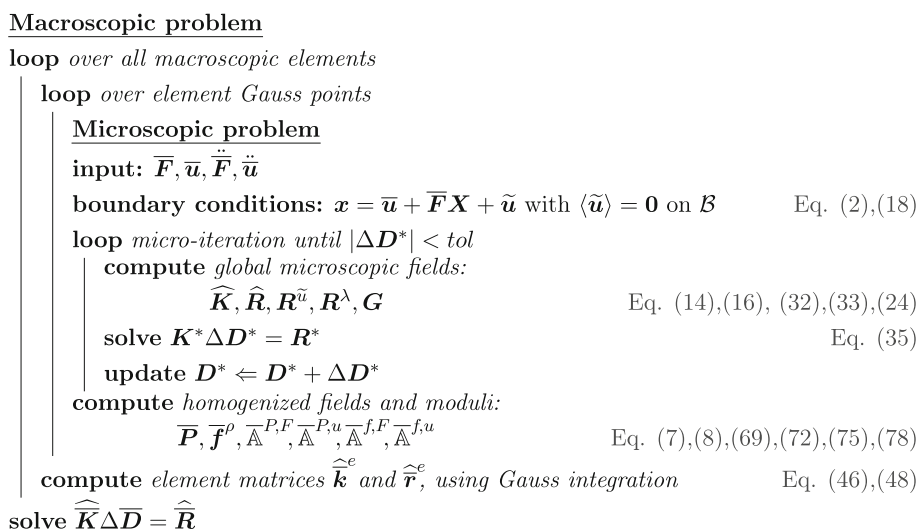
Derivation of $\bar{\mathbb{A}}^{f,u}$: Analogously, the derivative is rewritten as

$$\bar{\mathbb{A}}_{ik}^{f,u} = \frac{\partial \bar{f}_i^{\rho}}{\partial \ddot{u}_k} = \frac{\partial \langle \rho_0 \ddot{u}_i \rangle}{\partial \ddot{u}_k}. \quad (76)$$

Then, using (3) and FE discretization, the expression becomes

$$\bar{\mathbb{A}}_{ik}^{f,u} = \sum_{e=1}^{n_{\text{ele}}} \left(\frac{1}{V} \int_{\mathcal{B}^e} \rho_0 \delta_{ik} \, dV \right)$$

Fig. 3 Algorithm for single macroscopic iteration of the dynamic FE² framework with respective equation references. It should be noted that the overall structure of the standard FE procedure does not change, only some additional fields need to be computed. Furthermore, for the implementation of the microscopic problem, the macroscopic displacements $\bar{\mathbf{u}}$ may be omitted from the code. It is the second derivative $\ddot{\bar{\mathbf{u}}}$, computed in the macroscopic problem, which influences the microscopic results



$$+ \frac{1}{V} \frac{\alpha_1}{\Delta t^2} \int_{\mathcal{B}^e} \rho_0 N_{Pi}^e dV \frac{\partial \tilde{d}_p^e}{\partial \tilde{u}_k^e} \Bigg). \tag{77}$$

Taking into account the global abbreviations in Appendix 1 Tables 2, 3 and inserting (66), the modulus is derived as

$$\bar{\mathbb{A}}^{f,u} = \langle \rho_0 \rangle - \frac{1}{V} \frac{\alpha_1}{\Delta t^2} \mathbf{W}^{*T} \mathbf{K}^{*-1} \mathbf{W}^*. \tag{78}$$

Note that if $\bar{\alpha}_1$ and α_1 are equal to zero, which would be equivalent to a quasi-static calculation, the first tangent moduli in (69) take the same form as e.g. found in [40]. Here, the closed form moduli (69), (72), (75) and (78) extend this consistently to the dynamic regime. Note that for a comparable approach at small strains, most derivative terms are conceptually quite similar. Also the incorporation of the new kinematic constraint in terms of Lagrange multipliers can be considered analogous for small strains. An overview over the algorithm of the proposed framework is presented in Fig. 3.

5 Numerical analysis: layered structure

This section presents numerical studies as a proof of concept, as well as an initial analysis of different RVE choices. As it turns out, for dynamic homogenization the definition of RVE is even more complex than for quasi-static cases. Single-scale comparisons are calculated to assess the reliability of the homogenization framework. First, a rather arbitrary example is shown to analyze the macroscopic Newton iteration and demonstrate the quadratically converging algorithm, which is based on the tangent moduli derived in Sect. 4. Then the concept of a unit cell as RVE is analyzed under dynamic conditions. Finally, a comparison of two different displacement constraints, including the proposed one, is presented. All numerical examples make use of the Newmark scheme

with the parameters $\gamma = 0.5$ and $\beta = 0.25$, resulting in an unconditionally stable algorithm. For more details on time integration methods in the context of nonlinear FE methods see e.g. [66].

A one-dimensional model of a layered structure with the total length of L is investigated. The studied heterogeneous material consists of two alternating phases, a soft and light phase, and a stiff and heavy phase. Each phase has a length of l_M , a Young’s modulus E_1 and E_2 , and a density ρ_1 and ρ_2 , respectively. All calculations are run using $E_1 = 2 \cdot 10^3 \frac{\text{N}}{\text{mm}^2}$, $E_2 = 2 \cdot 10^5 \frac{\text{N}}{\text{mm}^2}$, $\rho_1 = 1 \cdot 10^3 \frac{\text{kg}}{\text{m}^3}$ and $\rho_2 = 1 \cdot 10^5 \frac{\text{kg}}{\text{m}^3}$. The Poisson’s ratio is chosen to be negligible, i.e. $\nu = 10^{-6}$, to enable a quasi-1D investigation. The left boundary is fixed, on the right end an impact load is applied in terms of a displacement boundary condition using the polynomial function $\bar{u}(t) = \frac{2^8 \bar{u}_{\max}}{T^8} (t)^4 (t - T)^4$, where \bar{u}_{\max} is the amplitude of the impact wave and T the duration in which the load is applied. Initially, the bar is at rest. The problem will be solved using both, a standard single-scale finite element problem referred to as direct numerical simulation (DNS), as well as the proposed dynamic FE² framework, c.f. Fig. 4 respectively. The DNS discretizes the microscopic phases at the macroscale into a large number of finite elements with a length of l_E . It thereby serves as overkill reference for the multiscale approach. The FE² simulations have a macroscopic element length of $l_{\bar{E}}$ and make use of the same element length l_E at the microscale for better direct comparability of the microscopic fields to the DNS. To approximate the displacement fields of the elements, linear shape functions and two Gauss points are used for all scales. As shown in Fig. 4b, each microscopic RVE calculation is associated to a single macroscopic integration point. The corresponding parameters for each simulation, regarding geometry, material parameters and loading will be listed in the caption of each figure.

Fig. 4 Illustration of the numerical calculations including, **a** a 1D single-scale FE Model, **b** the macroscopic model and the RVE of the FE² approach

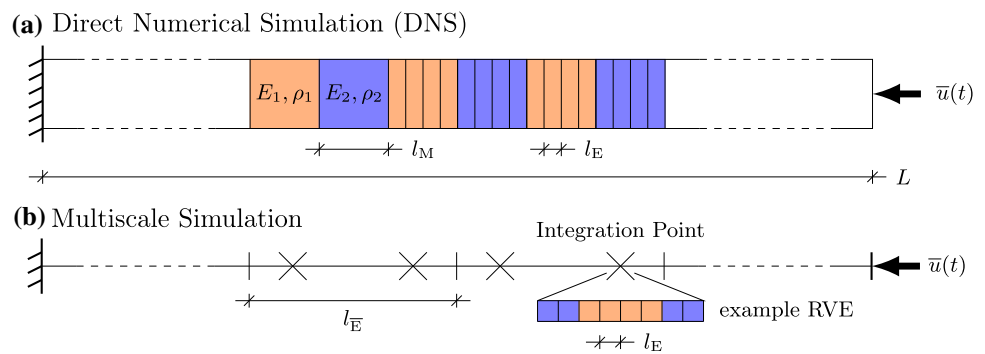
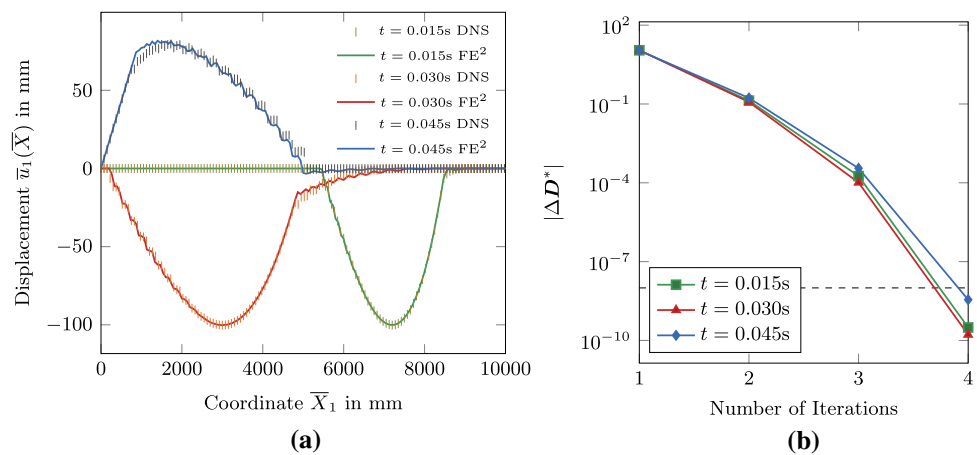


Fig. 5 Analysis of algorithmic consistency: **a** comparison of displacement fields, **b** convergence of the macroscopic Newton iteration with a tolerance of 10^{-8} . The simulation parameters are $L = 10,000$ mm, $l_M = 10$ mm, $l_E = 33.33$ mm, $\bar{u}_{\max} = 100$ mm, $T = 0.01$ s, $\Delta t = 5 \cdot 10^5$ s and basic unit cell type A as RVE



5.1 Consistency of numerical framework

This example analyzes the convergence behavior of the macroscopic Newton iteration. In Fig. 5a, the distribution of macroscopic displacement fields is shown at three different time instances for both, the DNS and the FE² calculation. As RVE, the basic unit cell of the type A (c.f. Fig. 6) is used. It can be seen, that the dynamic multiscale framework approximates the overall behavior well and even captures some of the smaller waves arising from the microstructure. A better representation of the wave propagation might be achieved by using finer time steps, but this would generally make the calculation converge faster as the initial values are already closer to the solution, defying the objective to properly test the tangent moduli. The convergence behavior for the three arbitrarily chosen time frames is depicted in Fig. 5b. Quadratic convergence of the norm of the updates of the nodal displacements $|\Delta D^*|$ is observed. This demonstrates that the macroscopic tangent moduli, incorporating both the microscale inertia forces as well as possible constraints, have been derived in a consistent manner. Note that in this example, locally strains appear of over 10% which exceed the range of small strains. However, due to the one-dimensionality of the problem, no significant influence from the finite strain setting can be expected.

5.2 Analysis of the unit cell concept under dynamic loading

For quasi-static homogenization simulations of periodic microstructures, it is known that the resulting macroscopic answer, as well as the corresponding microscopic fields are invariant with respect to the specific choice of unit cell, as long as an admissible periodic unit cell is chosen. In contrast to quasi-static cases, the distribution of the mass relative to the geometrical center matters in a dynamic setting. An extreme example is shown in Fig. 7, which compares the macroscopic displacement field at $t = 0.045$ s presented in the first example in Fig. 5a with a simulation using the basic unit cell type B as an RVE (c.f. Fig. 6). To properly measure the influence of different RVE choices on the FE² simulation, an objective error measure ϵ is considered. It is defined as average difference of the macroscopic displacement fields $\epsilon = \sum_i^{n_{\text{nodes}}} |\bar{u}_i^I(t_j) - \bar{u}_i^{II}(t_j)| / n_{\text{nodes}}$, where \bar{u}^I and \bar{u}^{II} stand for any two displacement signals that are being compared. This measure can be evaluated for each time step and thus, the average is once more computed over the number of time steps $\epsilon_{\text{time}} = \sum_j^{n_{\text{timesteps}}} \epsilon_j / n_{\text{timesteps}}$. Note, that due to the comparison of nodal displacements, a unitless error value obtained by dividing the difference by the reference value is problematic as the regarded value might be zero. Furthermore, a delay in the response may lead to relatively large

Fig. 6 Selection of RVE choices with different numbers of basic unit cells

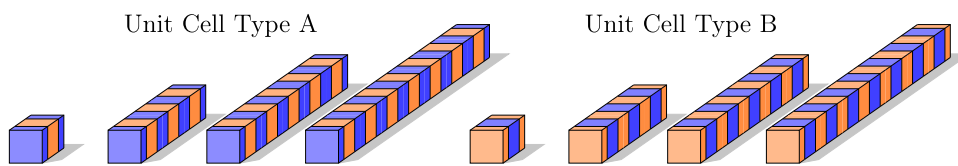
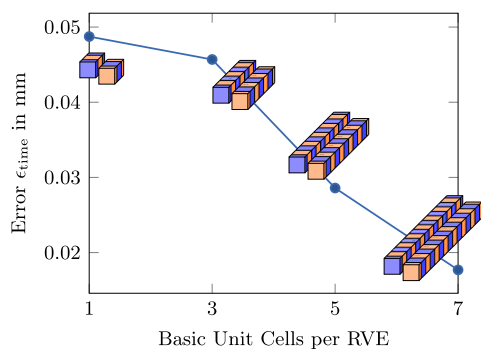
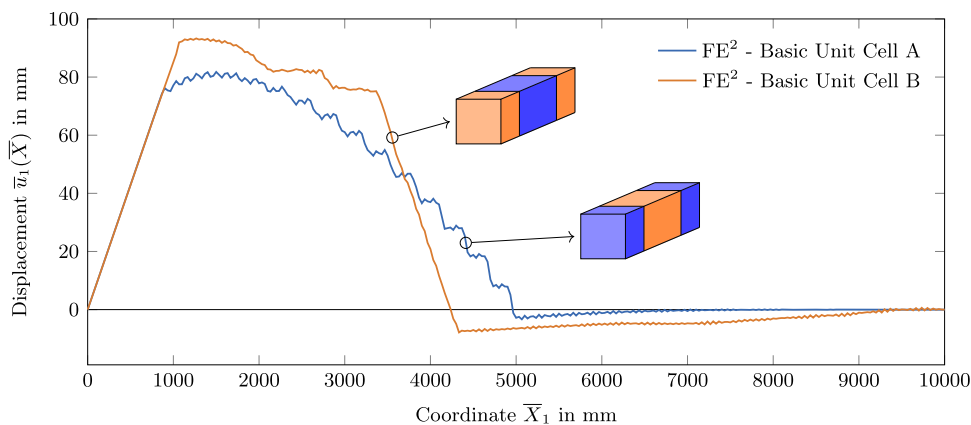
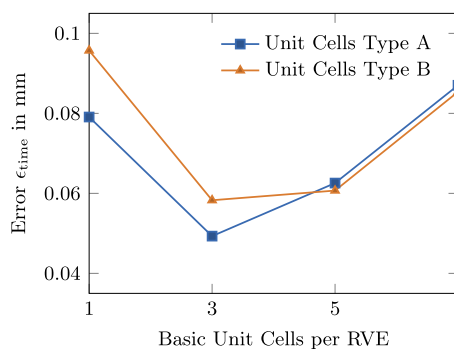


Fig. 7 Comparison of macroscopic displacement fields for two different RVEs with different basic unit cells types. The simulation parameters are $L = 10,000$ mm, $l_M = 10$ mm, $l_E = 33.33$ mm, $\bar{u}_{max} = 100$ mm, $T = 0.01$ s, $t = 0.045$ s and $\Delta t = 5 \cdot 10^{-5}$ s



(a)



(b)

Fig. 8 Analysis of different RVE choices: **a** direct comparison of RVEs with unit cell type A and B, for an increasing number of basic unit cells per RVE (the error is computed as difference between the response of the two unit cell types, not with respect to the DNS). **b** Error of unit cell

type A and B, compared to DNS as reference. The simulation parameters are $L = 10,000$ mm, $l_M = 2.5$ mm, $l_E = 20$ mm, $\bar{u}_{max} = 100$ mm, $T = 0.01$ s, $\Delta t = 5 \cdot 10^{-5}$ s, $n_{timesteps} = 400$

errors in the displacements summarizing over time even if the shape of the displacement wave is perfectly fine. Therefore, in principle it is difficult for dynamic problems to obtain a quantitative measure to evaluate the accuracy. The interpretation of the error value should therefore be done with caution, as the single value does not convey any information about the actual shape of the wave. However for the present analysis the considered error measure is sufficient to analyze the general trend. Figure 8 shows the calculated errors of different choices of the RVE. For the comparison, RVEs with multiple periods of the same unit cell type, as depicted in Fig. 6, were considered. Two effects can be observed: The first, presented in Fig. 8a, is that the difference in macroscopic displacements between different choices of unit cell type decreases, when the number of unit cells per RVE is increased. This means that the choice of particular basic unit cell type does not matter as

long as the RVE is chosen large enough. The second effect, shown in Fig. 8b, is that the error, computed as difference to the DNS reference, increases when the size of the RVE, relative to the macroscopic element length, gets too large. Then, errors resulting from a violation of the scale separation assumption are obtained. Generally, the second effect can be neglected, as calculations with RVE sizes larger than the macroscopic element length have little practical application when using FE^2 . At this point it is favorable to use domain decomposition approaches instead of a homogenization method in order to avoid the scale separation assumption.

5.3 Influence of displacement constraints

Finally the proposed displacement link $\bar{u} = \langle \mathbf{u} \rangle$ is analyzed for the examples in Fig. 8b, in comparison to the standard

Table 1 Number of time steps before either the simulation crashed (divergence of Newton iteration at microscale) or the intended complete set of 1000 time steps was successfully reached

Number of unit cells per RVE		1	3	5	7
Unit cell type	$\bar{\mathbf{u}}$ -link	Number of time steps			
A	$\bar{\mathbf{u}} = \langle \mathbf{u} \rangle$	1000	940	1000	1000
	$\tilde{\mathbf{u}}_{\text{corner}} = \mathbf{0}$	1000	671	634	1000
B	$\bar{\mathbf{u}} = \langle \mathbf{u} \rangle$	1000	456	1000	1000
	$\tilde{\mathbf{u}}_{\text{corner}} = \mathbf{0}$	944	420	192	166

Different choices of RVEs and constraints were analyzed

displacement link for quasi-static periodic homogenization, where the fluctuations at the RVE corner nodes is set to zero, i.e. $\tilde{\mathbf{u}}_{\text{corner}} = \mathbf{0}$. For the quasi-1D example analyzed here, this is equivalent to setting the integral over the surface equal to the corresponding macroscopic displacements, which has been taken into account in other dynamic homogenization schemes.

The first observation is, that using the proposed volume constraint $\bar{\mathbf{u}} = \langle \mathbf{u} \rangle$ results in a more robust framework in terms of stability of the Newton–Raphson iterations. Furthermore, slightly smaller error values are obtained compared to the DNS reference. Table 1 shows the number of time steps reached before either the calculations crashed (due to diverging Newton iterations at the microscale) or they were finished successfully after the intended complete set of 1000 time steps. Especially the calculations using the unit cell type B in combination with the zero fluctuations of the corner nodes, underperformed the other scenarios. To understand the difference between the performance of the displacement links, it is necessary to examine the behavior at the RVE level.

Here the examples with the RVEs consisting of three periods of the basic unit cell B are further analyzed. Figure 9 compares the microscopic displacements for four relevant time instances right before the peak of the input wave passes through the RVEs. More specifically, the differences between the microscopic displacement fields \mathbf{u} of an RVE and the respective macroscopic displacements $\bar{\mathbf{u}}$. To compare the DNS, an effective $\bar{\mathbf{u}}$ has been computed as the average displacement over the associated length. Thereby, the quality of the microscopic fields can be analyzed independently of the macroscopic displacements. With this, the two different displacement constraint options can be effectively compared with the reference solution obtained from DNS. The graphs show, that the fixed corner constraint leads to artificially increased displacement intensities at the microscale due to the constricted boundary. These increased displacements eventually lead to extreme deformations in single elements at the microscale, crashing the simulation. The proposed displacement volume constraint however, leads to a softer constraint which results in a more robust computation

while still enabling dynamic effects which agree well with the ones from the reference DNS. In the presented examples, the only rate-dependent influence are inertia forces. In cases where also rate-dependent material properties are included we expect the influence of different displacement constraints on the overall simulation to increase, in favor for the proposed volume constraint.

6 Numerical analysis: split Hopkinson bar

After presenting an analysis focused on the study of general properties of dynamic homogenization, this section shows the applicability of the framework to an engineering problem. A standard experiment to study material behavior under impact loading is therefore replicated, the split Hopkinson tension bar test, see e.g. [11,58]. By releasing a pre-strained steel bar, a loading pulse is transmitted to an aluminum input bar. The wave travels along the bar and through a specimen, which is sandwiched between the input and another aluminum bar called the output bar. Strain gauges in the two bars record the wave signal. By applying the elastic, uniaxial stress wave propagation theory to the split Hopkinson bar experiment, the time history of the forces and the displacements of the faces of the test specimen are calculated, in the following denoted as $\bar{\sigma}_1$ and $\bar{\sigma}_2$, cf. [28]. These are then used to approximate the stress and strain within the specimen in loading direction. A schematic visualization is presented in Fig. 10. As target material, a strain-hardening cementitious composite (SHCC) is chosen. This fiber-reinforced concrete exhibits an outstanding ductility and a pronounced energy dissipation under high strain rates. Therefore it is ideal as reinforcing layer to improve the impact resistance of structures [12]. The interpretation of experimentally measured data under dynamic conditions is difficult. Therefore there is a need for accurate simulations including inertia at the macro- and the microscale. In [58] a quite simplified microstructure was considered as RVE. Although a three-dimensional discretization of the RVE was taken into account, the multidimensional character with respect to mechanics was strongly limited by the fact that only one fiber in the direction of the main macroscopic traveling wave direction was taken into account. Therefore, in contrast to [58], here we consider an RVE with multiple fibers to more realistically reflect the three-dimensional nature of microscopic problems in real SHCC. In total, 13 randomly oriented fibers are included representing a more or less isotropic distribution of fiber orientations. First the applied micromechanical models and the chosen microstructure are presented. The macroscopic boundary value problem is shown and used to analyze the dynamic effects.

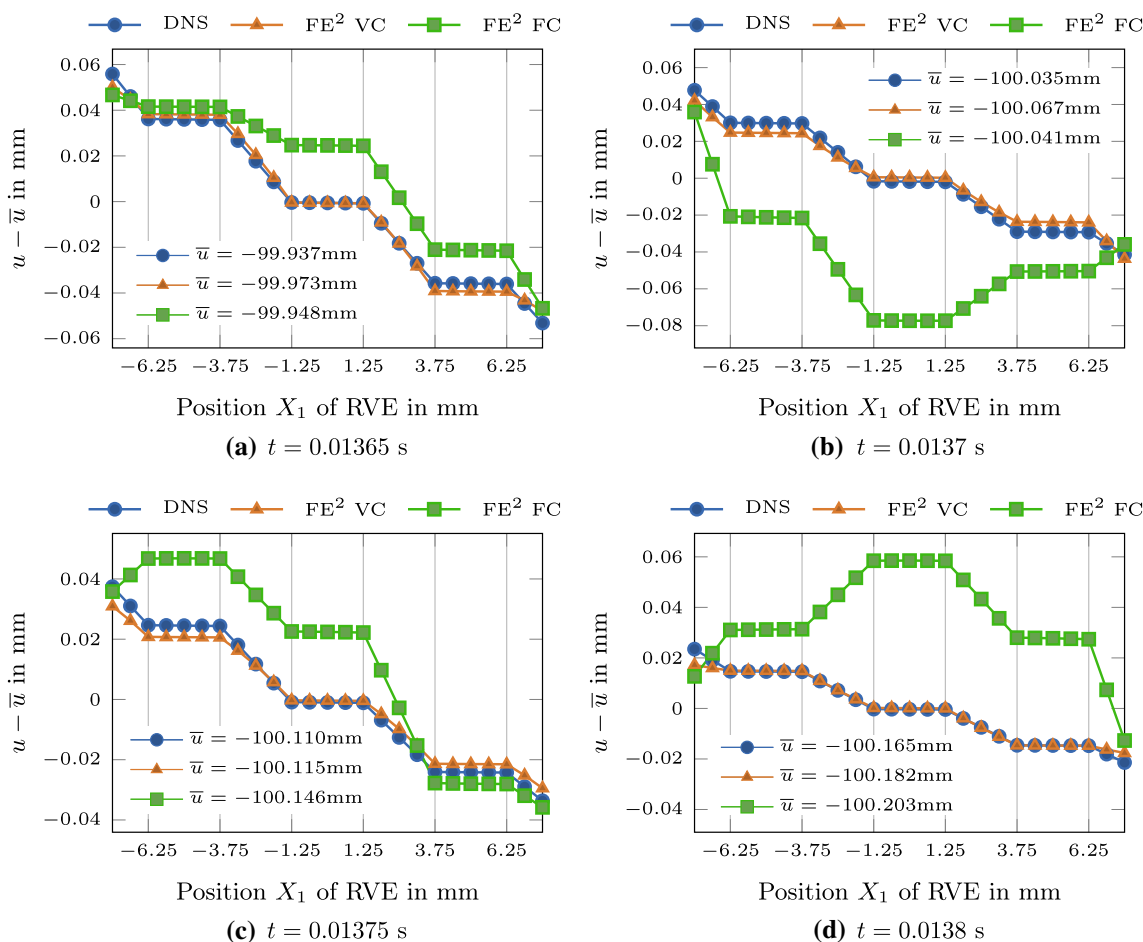


Fig. 9 Comparison of microscopic displacement fields obtained from the FE² simulations with the DNS. The displacements have been normalized by \bar{u} (for the DNS, average displacement) to analyze the quality of microscopic displacements more or less independent of the macroscopic displacements. The two different displacement links, the volume constraint (VC) and the fixed corners (FC) are analyzed. The simula-

tion parameters are $L = 10,000$ mm, $l_M = 2.5$ mm, $l_E = 20$ mm, $\bar{u}_{max} = 100$ mm, $T = 0.01$ s, $\Delta t = 5 \cdot 10^5$ s, location of the macroscale integration point $\bar{X}_1 = 7504, 23$ mm, section of the DNS displacement field from $\bar{X}_1 = 7496.25$ mm to $\bar{X}_1 = 7511.25$ mm, RVE with three periods of basic unit cell types B

6.1 Microscale problem

The microscale problem discretizes the fiber-reinforced concrete. Therefore the relevant micromechanical features need to be replicated. Before the first crack through the cementitious matrix, the concrete matrix itself dominates the material behavior of the composite. Once a crack has formed the fibers are engaged and bridge the crack. Finally, a crack will open when the fibers are pulled out. The fiber properties as well as the pullout behavior are shown to be rate dependent [9,11]. To capture these micromechanical effects two main models are required: (i) a model for the concrete matrix, including cracking and (ii) a representation for the embedded fibers. The concrete is represented as a first approximation by a standard Neo–Hooke material law. The complex compressive behavior of concrete is neglected as only tensile loading

is considered within this example. A realistic representation of the crack development is not within the scope of this work. Therefore, to represent the matrix cracking, a simple erosion method is implemented. It sets the material stiffness of an integration point close to zero, once the stress in loading direction surpasses a critical value σ_{cr} . The fibers are represented by a linear truss element, sharing the nodes with the matrix mesh. This allows for a 1D effective material law to be applied, capturing the complex material behavior of the fiber as well as that of the fiber–matrix bond. However, the forces are thus not transferred to the matrix continuously, leading to stress concentrations at the nodes resulting in spurious crack patterns. Therefore, the crack path in the matrix is here defined in advance. The chosen material model uses a general 1D Neo–Hookean material law with an additional strain rate sensitivity of the stress as well as a damage formu-

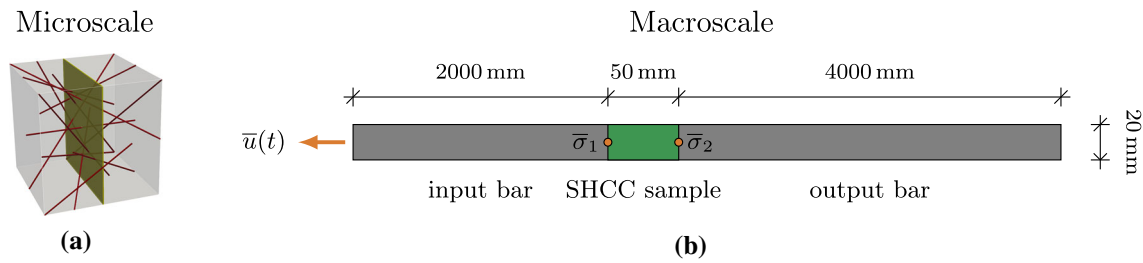


Fig. 10 Schematic visualization of the multiscale split Hopkinson tension bar simulation. **a** Depicts the RVE, **b** the macroscopic problem

lation, cf. [58]. The stress in terms of the first Piola–Kichhoff stress tensor is given by $P = \frac{1}{2}E(F - \frac{1}{F})(1 + \Omega)(1 - D)$ where E is the Young’s modulus, Ω denotes the dynamic increase which takes on only positive values, and D is the damage value which takes on values from 0 to 1. The dynamic increase function Ω is defined by a logarithmic function, which depends on the rate of the deformation gradient \dot{F} . For values of $\dot{F} \geq \alpha^{\text{II}}$, it is defined as $\Omega = \alpha^{\text{I}} \ln[\frac{\dot{F}}{\alpha^{\text{II}}}]$ otherwise it is zero, i.e. no dynamic increase for rates lower than α^{II} . The exponential damage formulation is given by $D = D_{\infty}(1 - \exp(-(\frac{\psi_D}{D_{\text{rate}}})^{D_{\text{shape}}}))$. The damage value D is determined by the effective energy considered for damage ψ_D . It is defined as the current maximum value of the strain energy function ψ_0 . The damage algorithm is therefore classified as a discontinuous damage approach. The damage evolution is controlled by three parameters. D_{∞} defines the maximum damage reached, $D_{\text{rate}} > 0$ sets the velocity of the damage evolution, and D_{shape} modifies the shape of the function.

As RVE, a cubic body with an edge length of 1 mm is chosen, see Fig. 10a. A crack face perpendicular to the loading direction is located in the center, splitting the matrix in two halves, which are connected by a number of 13 randomly oriented fibers. The concrete matrix is modeled by brick elements, whereas in the center, the feature for cracking is included to represent a possible crack through the matrix. This microstructure fulfills minimal geometric requirements to reproduce the relevant micromechanical processes of SHCC. More complex structures are only of value once advanced micromechanical models are utilized. In the subsequent simulations the following material parameters are used: for the concrete matrix $E = 29 \text{ kN/mm}^2$, $\nu = 0.3$, and $\rho_0 = 2100 \text{ kg/m}^3$, additionally for the crack $E_{\text{cr}} = 10^{-3} \text{ kN/mm}^2$ and $\sigma_{\text{cr}} = 5 \text{ kN/mm}^2$, for the fiber model $E = 40 \text{ kN/mm}^2$, $A = 0.00385 \text{ mm}^2$, $\rho_0 = 980 \text{ kg/m}^3$, $D_{\infty} = 0.9982$, $D_{\text{shape}} = 0.36$, $D_{\text{rate}} = 0.2$, $\alpha^{\text{I}} = 0.08$, and $\alpha^{\text{II}} = 0.51$.

6.2 Macroscopic boundary value problem

The macroscale represents the experimental setup of the split Hopkinson tension bar. The cylindrical equipment

and SHCC sample are discretized by truss elements. Standard elements are used to simulate the aluminum input and output bars, the two-scale homogenization framework is applied to model only the SHCC specimen. A sketch of the setup is shown in Fig. 10b. All elements have a length of 10 mm. To simulate the experimental loading conditions a piece-wise polynomial function \bar{u}^{BC} is chosen. The load is applied as a boundary displacement. The three parts are defined as $\bar{u}^{\text{I}}(t) = \frac{14}{275} t v_c (\frac{2t}{t_{\text{vc}}})^3$, $\bar{u}^{\text{II}}(t) = \frac{t v_c}{275} [7(\frac{2t}{t_{\text{vc}}})^8 - 12(\frac{2t}{t_{\text{vc}}})^7 + 16(\frac{2t}{t_{\text{vc}}})^6 + 19 - \frac{34}{3}(\frac{2t}{t_{\text{vc}}})^{-1}]$ and $\bar{u}^{\text{III}}(t) = v_c(t - \frac{529}{825} t_{\text{vc}})$. The transitions between the respective functions are at $\bar{u}^{\text{I}}(0.592 t_{\text{vc}}) = \bar{u}^{\text{II}}(0.592 t_{\text{vc}})$ and $\bar{u}^{\text{II}}(t_{\text{vc}}) = \bar{u}^{\text{III}}(t_{\text{vc}})$.

The function describes the pulse, which is characterized by two phases. First the acceleration phase and second a phase of constant velocity. The two parameters of the function t_{vc} and v_c , define respectively the time when the transition from the first to the second phase is reached and the constant velocity.

6.3 Results

By using the presented microstructure in combination with the split Hopkinson tension bar simulation, the capabilities of the developed framework to analyze material behavior of composites under dynamic loading are illustrated. Following the experimental procedure, the stress signals $\bar{\sigma}_1$ and $\bar{\sigma}_2$ of the nodes at the specimen interfaces is averaged as $\bar{\sigma}$. The stress is then plotted against an approximated specimen strain, computed by the difference of displacement of the interfaces divided by the specimen length. First a quasi-static simulation is compared to the dynamic response, shown in Fig. 11. A clear increase in the dynamic simulation is observed. In addition, a shift is visible from the sudden drop of stress under quasi static loading, due to the homogeneous stress state, to a more gradual stress increase under dynamic conditions, mimicking the multiple cracking behavior of SHCC. Then, to understand the origin of the dynamic increase, two parameter studies are conducted. In Fig. 12, the strain rate sensitivity of the fibers is varied. Clearly, the overall stress response is increased by an increase in α^{I} . In

Fig. 11 Quasi-static and dynamic results of the split Hopkinson tension bar simulation. The zoom shows the initial cracking of the matrix

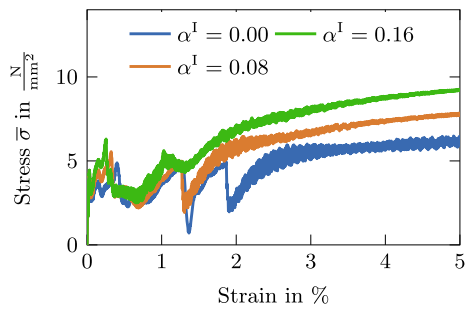
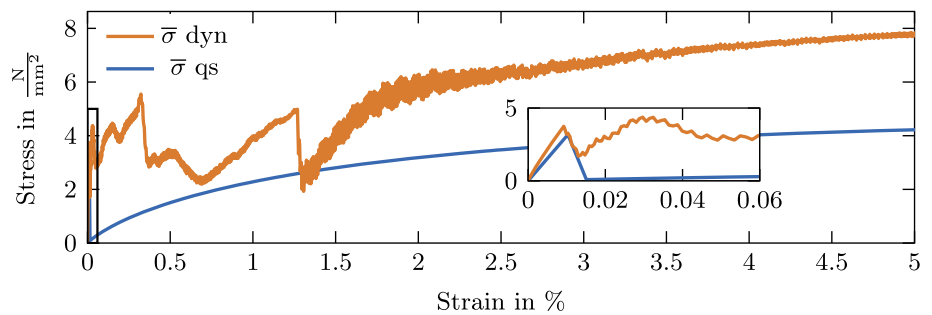


Fig. 12 Variation of the strain rate sensitivity α^I

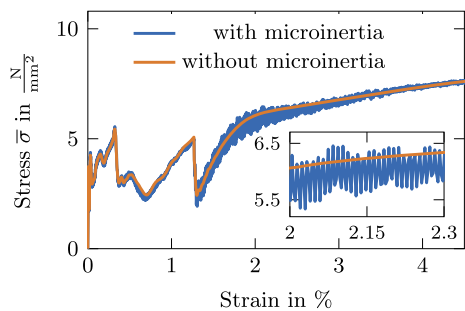


Fig. 13 Influence of microinertia on the macroscopic response

addition, the unsteady phase of multiple cracking is completed at smaller overall strains, due to the effective increase in fiber stiffness. A similar effect is observed when comparing microstructures with random fiber direction to perpendicular fibers in loading direction. The fibers at an angle to the applied load result in the softer macroscopic response, c.f. [58]. In Fig. 13, the focus is on the influence of the microinertia. It is evident that the main dynamic influences of this example are the structural inertia and the strain rate sensitivity of the fiber pullout. The microscopic inertia, in contrast to the earlier example of the layered structure in Sect. 5, does not appear to have a significant influence on the macroscopic stress. As the chosen microstructure only allows for moderate dynamic activity, this is not surprising. However with more advanced micromechanical models this might change.

7 Conclusion

In this paper, a general purpose, consistent, two-scale homogenization framework for dynamics at the macro- and microscale was proposed in the sense of the FE² method. The novelty of this framework lays in its generality. The framework does not include any simplifications such as linearized strains, explicit time integration or partly quasi-static scenarios. The only assumption taken into account is a sufficiently pronounced scale separation, which is anyway essential requirement of any FE² approach. Therefore, it enables the simulation of various structural problems of complex micro-heterogeneous materials under dynamic loading such as impact. Furthermore, the derived formulations are compatible with standard FE² architecture. The main aspects are: (i) the incorporation of the complete balance of momentum at the micro- and macroscale including inertia forces, (ii) extended microscopic boundary conditions resulting in a more robust scheme and giving the possibility for non-periodic RVE boundaries, (iii) a finite-strain formulation enabling the simulation of a wide range of macro- and micro-mechanical phenomena, and (iv) the derivation of consistent macroscopic tangent moduli ensuring quadratically converging macroscopic iterations. The presented results on different choices of RVEs show that different admissible unit cells of a periodic microstructure lead also to a different mechanical response - even if periodic boundary conditions are employed. This is in contrast to quasi-static scenarios. However, these results should not entail that the most basic unit cell is necessarily a bad choice for a simulation, but the specific choice of this basic unit cell is not unique. In addition, a more complex simulation of a split Hopkinson tension test on an SHCC specimen was presented. The example at hand, compared to the simplified microstructure in [58], exhibits a softer macroscopic response, as not all fibers are oriented in loading direction. This is apparent due to the more pronounced phase of multiple cracking up to 1.5% strain. The example shows the capability of the multiscale framework to further the understanding of experimental material behavior under impact.

Acknowledgements The authors gratefully acknowledge financial support from the German Research Foundation (DFG) within project B1 of the Training Research Group (GRK) 2250 “Mineral-Bonded Composites for Enhanced Structural Impact Safety”. Furthermore, fruitful discussions with Celia Reina (University of Pennsylvania) are greatly appreciated.

Funding Open Access funding enabled and organized by Projekt DEAL.

Open Access This article is licensed under a Creative Commons Attribution 4.0 International License, which permits use, sharing, adaptation, distribution and reproduction in any medium or format, as long as you give appropriate credit to the original author(s) and the source, provide a link to the Creative Commons licence, and indicate if changes were made. The images or other third party material in this article are included in the article’s Creative Commons licence, unless indicated otherwise in a credit line to the material. If material is not included in the article’s Creative Commons licence and your intended use is not permitted by statutory regulation or exceeds the permitted use, you will need to obtain permission directly from the copyright holder. To view a copy of this licence, visit <http://creativecommons.org/licenses/by/4.0/>.

Appendix: Matrix abbreviations

See Tables 2 and 3.

Table 2 Overview of the used fields at element and global level, with n_{edf} : number of DOF at element level and n_{dm} : spatial dimension

Global		Element
Definition	Size	
$\mathbf{K} = \mathbf{A} \mathbf{k}^e$	$n_{\text{edf}} \times n_{\text{edf}}$	$k_{PQ}^e = \int_{\mathcal{B}^e} B_{ijP}^e \mathbb{A}_{ijkl} B_{klQ}^e dV$
$\mathbf{L} = \mathbf{A} \mathbf{l}^e$	$n_{\text{edf}} \times n_{\text{dm}}^2$	$l_{Pij}^e = \int_{\mathcal{B}^e} B_{klP}^e \mathbb{A}_{klij} dV$
$\mathbf{M} = \mathbf{A} \mathbf{m}^e$	$n_{\text{edf}} \times n_{\text{edf}}$	$m_{PQ}^e = \int_{\mathcal{B}^e} N_{Pi}^e \rho_0 N_{Qi}^e dV$
$\mathbf{W} = \mathbf{A} \mathbf{w}^e$	$n_{\text{edf}} \times n_{\text{dm}}$	$w_{Pi}^e = \int_{\mathcal{B}^e} \rho_0 N_{Pi}^e dV$
$\mathbf{Z} = \mathbf{A} \mathbf{z}^e$	$n_{\text{edf}} \times n_{\text{dm}}^2$	$z_{Pij}^e = \int_{\mathcal{B}^e} \rho_0 N_{Pi}^e X_j dV$
$\mathbf{G} = \mathbf{A} \mathbf{g}^e$	$n_{\text{edf}} \times n_{\text{dm}}$	$g_{Pi}^e = \int_{\mathcal{B}^e} N_{Pi}^e dV$
\mathbf{V}	$n_{\text{dm}}^2 \times n_{\text{dm}}$	$V_{ijk} = \rho_0 \delta_{ik} X_j$
\mathbb{Y}	$n_{\text{dm}}^2 \times n_{\text{dm}}^2$	$\mathbb{Y}_{ijkl} = \rho_0 \delta_{ik} X_l X_j$

Table 3 Overview of the extended fields, with n_{edf} : number of DOF at element level, n_{igr} : number of DOF of Lagrange constraint and n_{dm} : spatial dimension

Matrix	Size
$\mathbf{D}^* = \left[\tilde{\mathbf{D}}^T \mid \boldsymbol{\lambda}^T \right]^T$	$(n_{\text{edf}} + n_{\text{igr}}) \times 1$
$\mathbf{L}^* = \left[\mathbf{L}^T + \frac{\alpha}{\Delta t^2} \mathbf{Z}^T \mid \mathbf{0} \right]^T$	$(n_{\text{edf}} + n_{\text{igr}}) \times n_{\text{dm}}^2$
$\mathbf{L}^{\bar{*}} = \left[\mathbf{L}^T + \frac{\bar{\alpha}}{\Delta t^2} \mathbf{Z}^T \mid \mathbf{0} \right]^T$	$(n_{\text{edf}} + n_{\text{igr}}) \times n_{\text{dm}}^2$
$\mathbf{W}^* = \left[\mathbf{W}^T \mid \mathbf{0} \right]^T$	$(n_{\text{edf}} + n_{\text{igr}}) \times n_{\text{igr}}$
$\mathbf{K}^* = \left[\begin{array}{c c} \mathbf{K} + \frac{\alpha}{\Delta t^2} \mathbf{M} & \mathbf{G} \\ \hline \mathbf{G}^T & \mathbf{0} \end{array} \right]$	$(n_{\text{edf}} + n_{\text{igr}}) \times (n_{\text{edf}} + n_{\text{igr}})$

References

- Bensoussan A, Lions J-L, Papanicolaou G (1978) Asymptotic analysis for periodic structures. North-Holland Publishing Company, Amsterdam
- Bertsekas DP (1996) Constrained optimization and Lagrange multiplier methods. Athena Scientific, New York
- Blanco PJ, Sánchez PJ, de Souza Neto EA, Feijóo RA (2016) Variational foundations and generalized unified theory of RVE-based multiscale models. Arch Comput Methods Eng 23:191–253
- Blanco PJ, Clausse A, Feijóo RA (2017) Homogenization of the Navier–Stokes equations by means of the multi-scale virtual power principle. Comput Methods Appl Mech Eng 315:760–779
- Brûlé S, Javelaud EH, Enoch S, Guenneau S (2014) Experiments on seismic metamaterials: molding surface waves. Phys Rev Lett 112:133901
- Coenen EWC, Kouznetsova VG, Geers MGD (2012) Novel boundary conditions for strain localization analyses in microstructural volume elements. Int J Numer Methods Eng 90:1–21
- Craster RV, Kaplunov J, Pichugin AV (2010) High-frequency homogenization for periodic media. Proc R Soc A 466:2341–2362
- Cummer SA, Schurig D (2007) One path to acoustic cloaking. New J Phys 9:45
- Curosu I (2018) Influence of fiber type and matrix composition on the tensile behavior of strain-hardening cement-based composites (SHCC) under impact loading. Doctoral dissertation, Schriftenreihe des Instituts für Baustoffe Heft 2018/1, V. Mechtcherine (Hrsg.), Technische Universität Dresden, 2018. ISBN 978-3-86780-555-1
- Curosu I, Mechtcherine V, Millon O (2016) Effect of fiber properties and matrix composition on the tensile behavior of strain-hardening cement-based composites (SHCCs) subject to impact loading. Cem Concr Res 82:23–35
- Curosu I, Mechtcherine V, Forni D, Cadoni E (2017) Performance of various strain-hardening cement-based composites (SHCC) subject to uniaxial impact tensile loading. Cem Concr Res 102:16–28
- Curosu I, Mechtcherine V, Hering M, Curbach M (2019) Mineral-bonded composites for enhanced structural impact safety—overview of the format, goals and achievements of the research training group GRK 2250. In: 10th international conference on fracture mechanics of concrete and concrete structures. <https://doi.org/10.21012/FC10.235408>
- de Souza Neto EA, Feijóo RA (2010) Variational foundations of large strain multiscale solid constitutive models: kinematical formulation, Chapter 9. Wiley, London, pp 341–378

14. de Souza Neto EA, Blanco PJ, Sánchez PJ, Feijóo RA (2015) An RVE-based multiscale theory of solids with micro-scale inertia and body force effects. *Mech Mater* 80:136–144
15. Feyel F (1999) Multiscale FE² elastoviscoplastic analysis of composite structures. *Comput Mater Sci* 16:344–354
16. Fish J, Shek K (1999) Finite deformation plasticity for composite structures: computational models and adaptive strategies. *Comput Methods Appl Mech Eng* 172:145–174
17. Fish J, Chen W, Nagai G (2002) Non-local dispersive model for wave propagation in heterogeneous media: multi-dimensional case. *Int J Numer Methods Eng* 54:347–63
18. Geers MGD, Kouznetsova VG, Matouš K, Yvonnet J (2017) Homogenization methods and multiscale modeling: nonlinear problems. Wiley, London, pp 1–34
19. Hill R (1972) On constitutive macro-variables for heterogeneous solids at finite strain. *Proc R Soc A* 326:131–147
20. Hu R, Oskay C (2018) Spatial-temporal nonlocal homogenization model for transient anti-plane shear wave propagation in periodic viscoelastic composites. *Comput Methods Appl Mech Eng* 342:1–31
21. Hu R, Oskay C (2019) Multiscale nonlocal effective medium model for in-plane elastic wave dispersion and attenuation in periodic composites. *J Mech Phys Solids* 124:220–243
22. Hui T, Oskay C (2014) A high order homogenization model for transient dynamics of heterogeneous media including micro-inertia effects. *Comput Methods Appl Mech Eng* 273:181–203
23. Irving JH, Kirkwood JG (1950) The statistical mechanical theory of transport processes. IV. The equation of hydrodynamics. *J Chem Phys* 18:817
24. Kadic M, Bückmann T, Schittny R, Wegener M (2015) Experiments on cloaking in optics, thermodynamics and mechanics. *Philos Trans R Soc A* 373:20140357
25. Karamnejad A, Sluys LJ (2014) A dispersive multi-scale crack model for quasi-brittle heterogeneous materials under impact loading. *Comput Methods Appl Mech Eng* 278:423–444
26. Kettenbeil C, Ravichandra G (2018) Experimental investigation of the dynamic behavior of metaconcrete. *Int J Impact Eng* 111:199–207
27. Khajehtourian R, Hussein MI (2014) Dispersion characteristics of a nonlinear elastic metamaterial. *AIP Adv* 4:124308
28. Kolsky H (1949) An investigation of the mechanical properties of materials at very high rates of loading. *Proc Phys Soc Lond Sect B* 62(11):676–700
29. Li J, Chan CT (2004) Double-negative acoustic metamaterial. *Phys Rev E* 70(5):055602
30. Liu C, Reina C (2016a) Discrete averaging relations for micro to macro transition. *J Appl Mech* 83(8):081006
31. Liu C, Reina C (2016b) Discrete averaging relations for micro to macro transition. *J Appl Mech* 83(8):081006
32. Liu C, Reina C (2017) Variational coars-graining procedure for dynamic homogenization. *J Mech Phys Solids* 104:187–206
33. Liu C, Reina C (2018) Dynamic homogenization of resonant elastic metamaterials with space/time modulation. *Comput Mech* 64(1):147–161
34. Liu Z, Zhang X, Mao Y, Zhu YY, Yang Z, Chan CT, Sheng P (2000) Locally resonant sonic materials. *Science* 289(5485):1734–1736
35. Manadapu KK, Sengupta A, Papadopoulos P (2012) A homogenization method for thermomechanical continua using extensive physical quantities. *Proc R Soc A* 468:1696–1715
36. Mandel J (1971) *Plasticité classique et viscoplasticité*. Springer, Udine
37. Mei J, Liu Z, Wen W, Sheng P (2006) Effective mass density of fluid–solid composites. *Phys Rev Lett* 96:024301
38. Mercer B, Mandadapu KK, Papadopoulos P (2016) Homogenization of high-frequency wave propagation in linearly elastic layered media using a continuum Irving–Kirkwood theory. *Int J Solids Struct* 96:162–172
39. Miehe C (1996) Numerical computation of algorithmic (consistent) tangent moduli in large-strain computational inelasticity. *Comput Methods Appl Mech Eng* 134(3):223–240
40. Miehe C, Schotte J, Schröder J (1999) Computational micro-macro transitions and overall moduli in the analysis of polycrystals at large strains. *Comput Mater Sci* 16:372–382
41. Milton GW, Willis JR (2007) On modifications of Newton’s second law and linear continuum elastodynamics. *Proc R Soc A* 463:855–880
42. Milton GW, Willis JR (2010) Minimum variational principles for time-harmonic waves in a dissipative medium and associated variational principles of Hashin–Shtrikman type. *Proc R Soc A Math Phys Eng Sci* 466(2122):3013–3032
43. Miniaci M, Krushynska A, Bosia F, Pugno NM (2016) Large scale mechanical metamaterials as seismic shields. *New J Phys* 18:083041
44. Mitchell SJ, Pandolfi A, Ortiz M (2016) Effect of brittle fracture in a metaconcrete slab under shock loading. *J Eng Mech* 142(4):04016010
45. Molinari A, Mercier S (2001) Micromechanical modelling of porous materials under dynamic loading. *J Mech Phys Solids* 49:1497–1516
46. Moulinec H, Suquet P (1998) A numerical method for computing the overall response of nonlinear composites with complex microstructure. *Comput Methods Appl Mech Eng* 157:69–94
47. Nassar H, He Q-C, Auffray N (2015) Willis elastodynamic homogenization theory revisited for periodic media. *J Mech Phys Solids* 77:158–178
48. Nassar H, He Q-C, Auffray N (2016) On asymptotic elastodynamic homogenization approaches for periodic media. *J Mech Phys Solids* 88:274–290
49. Nemat-Nasser S, Srivastava A (2011) Overall dynamic constitutive relations of layered elastic composites. *J Mech Phys Solids* 59(10):1953–1965
50. Newmark NM (1959) A method of computation for structural dynamics. *J Eng Mech* 85:67–94
51. Pham K, Kouznetsova VG, Geers MGD (2013) Transient computational homogenization for heterogeneous materials under dynamic excitation. *J Mech Phys Solids* 61:2125–2146
52. Roca D, Lloberas-Valls O, Cante J, Oliver J (2018) A computational multiscale homogenization framework accounting for inertia effects: application to acoustic metamaterials modelling. *Comput Methods Appl Mech Eng* 330:415–446
53. Sartori C, Mercier S, Jacques N, Molinari A (2015) Constitutive behavior of porous ductile materials accounting for micro-inertia and void shape. *Mech Mater* 80:324–339
54. Schröder J (2013) *Plasticity and beyond—microstructures, crystal-plasticity and phase transitions* CISM Lecture Notes 550, Schröder J, Hackl K (eds) Chapter A numerical two-scale homogenization scheme: the FE²-method. Springer, London
55. Smit R, Brekelmans W, Meijer H (1998) Prediction of the mechanical behavior of nonlinear heterogeneous systems by multi-level finite element modeling. *Comput Methods Appl Mech Eng* 155:181–192
56. Sridhar A, Kouznetsova VG, Geers MGD (2018) A general multiscale framework for the emergent effective elastodynamics of metamaterials. *J Mech Phys Solids* 111:414–433
57. Tamsen E, Weber W, Balzani D (2018) First steps towards the direct micro–macro simulation of reinforced concrete under impact loading. *Proc Appl Math Mech* 18(1):e201800181
58. Tamsen E, Curosu I, Mechtcherine V, Balzani D (2020) Computational micro-macro analysis of impact on strain-hardening cementitious composites (SHCC) including microscopic inertia. *Materials* 13:4934

59. Terada K, Hori M, Kyoyac T, Kikuchi N (2000) Simulation of the multi-scale convergence in computational homogenization approaches. *Int J Solids Struct* 37:2285–2311
60. van Nuland TFW, Silva PB, Sridhar A, Geers MGD, Kouznetsova VG (2019) Transient analysis of nonlinear locally resonant metamaterials via computational homogenization. *Math Mech Solids* 24(10):3136–3155
61. Wang Z-P, Sun CT (2002) Modeling micro-inertia in heterogeneous materials under dynamic loading. *Wave Motion* 36:473–485
62. Willis JR (1981) Variational principles for dynamic problems for inhomogeneous elastic media. *Wave Motion* 3:1–11
63. Willis JR (1997) *Dynamics of composites*. Springer, Vienna
64. Willis JR (2009) Exact effective relations for dynamics of a laminated body. *Mech Mater* 41:385–393
65. Willis JR (2012) The construction of effective relations for waves in a composite. *C R Méc* 340(4):181–192
66. Wriggers P (2008) *Nonlinear finite element methods*. Springer, Berlin
67. Zhou X, Hu G (2009) Analytic model of elastic metamaterials with local resonance. *Phys Rev B* 79:195109

Publisher's Note Springer Nature remains neutral with regard to jurisdictional claims in published maps and institutional affiliations.